SANDIA REPORT

SAND97–8280 • UC–721
Unlimited Release
Printed August 1997

Cryocycling of Energetic Materials: Final Report

S. Griffiths, J. Handrock, D. Kasberg, J. Lipkin, R. Nilson, V. Revelli,
L. Weingarten and L. Whinnery

Edited by:
J. Lipkin

Sandia National Laboratories

Cryocycling of Energetic Materials: Final Report

S. Griffiths and R. Nilson
Mechanics & Simulation of MFG Processes Department

J. Handrock, V. Revelli and L. Weingarten
Structural & Thermomechanical Modeling Department

D. Kasberg
GTS Engineering Department

J. Lipkin
Environmental Technology Applications Department

L. Whinnery
Materials Processing Department
Sandia National Laboratories
Livermore, CA 94550

Edited by

J. Lipkin
Environmental Technology Applications Department
Sandia National Laboratories
Livermore, CA 94550

ABSTRACT

The Cryocycling of Energetic Materials Project was executed in the period FY'94-96 as a Life Cycle Engineering activity in the Memorandum of Understanding (MOU) on advanced conventional munitions. This MOU is an agreement between the Departments of Energy and Defense (Office of Munitions) that facilitates the development of technologies of mutual interest to the two Departments. The cryocycling process is a safe, environmentally friendly, and cost effective means of rubblizing bulk energetic materials so that they can be easily reused in a variety of new products. For this reason, cryocycling of excess solid energetic materials is one of the recycle/reuse strategies under study for demilitarized munitions in the Departments of Energy and Defense. These strategies seek to minimize the environmental damage associated with disposal of decommissioned energetic materials. In addition, they encourage technologies that can be used to

derive economic benefit from reuse/reapplication of materials that would otherwise be treated as hazardous wastes

This page intentionally left blank

CONTENTS

ILLUSTRATIONS

ILLUSTRATIONS (continued)

TABLES

8

No.		Page

Cryocycling of Energetic Materials: Final Report

INTRODUCTION

Background - Disposal of Excess Weapon Systems

The military services in the US, as well as in many foreign nations, possess large inventories of excess munitions containing a variety of energetic materials (i.e., propellants and explosives). As these items are demilitarized, a pressing need has developed to identify recycle and reuse applications for these energetic materials. Much of this material is currently destroyed as hazardous waste using Open-Burn/Open-Detonation (OB/OD) or incineration. As the name suggests, OB/OD is an uncontrolled thermal treatment process that produces largely unknown atmospheric emissions. For this reason, current and pending environmental regulations will almost certainly limit the use of this option in the future. At the same time, while incineration is a viable disposal option, it is expensive and not widely accepted by the public. All US military services are thus actively seeking alternative disposal methods for energetic materials. Many of the methods under consideration involve controlled destruction by thermal techniques. Such options, however, do not take advantage of the energetic content of the material. [1-3]

It is clear that any new disposal method must satisfy environmental regulations and take into account the following key processing steps

- removal of the energetic material from its protective case,
- size reduction,
- decomposition or recovery of the energetic components, and
- identification of all waste streams.

Although much work has been directed at decomposition or recovery of the energetic ingredients, comparatively less effort has been aimed at removal or particle size reduction.[1] These steps are essential for implementing recycle/reuse options. It is important to note that recycle/reuse options are especially attractive because they can return valuable assets to the nation's economy both by minimizing the generation of hazardous waste streams (e.g., air and ground pollution) and by creating new products in the commercial sector.[2] As an example, environmentally benign commercial reuse possibilities for solid rocket motor propellants that have been size reduced range from incorporation into explosives for mining to source material for high-value sporting powders. When the explosives detonate in these products, the resulting chemical emissions are mostly carbon dioxide and water.

Cryocycling - Technology and Process Description

Cryocycling is a safe and environmentally friendly technique for reducing the size of bulk energetic materials. In the cryocycling process, solid propellants and explosives are subjected to repeated thermal cycles between ambient and cryogenic temperatures. Fractures develop in the material during both the freezing and warming phases of the process, and, as these fractures

intersect during repeated cycling, the bulk material is reduced to relatively uniform sized rubble. For example, bulk nitrocellulose/nitroglycerin based propellants are typically reduced to fragments on the order of 6-10 mm size after 3-4 cryocycles. This size range allows a direct reuse of this propellant in new explosive products. Indeed, one of the advantages of cryocycling is that it preserves the energetic value of the material, and thus allows use of straightforward recycle/reuse options in the commercial explosives industry. In demonstrations carried out to date, nearly 5000 pounds of propellant from more than 250 excess rocket motors have been incorporated into new commercial explosives that have been field tested at full scale.[1,3]

The concept and mechanics of cryocycling are deceptively straightforward. Contact with liquid nitrogen induces thermal gradients in the bulk of the material. These temperature gradients produce stress gradients within the material. Stress relieving cracks are then formed when internal stresses exceed local material strength. Additional cracking also occurs upon warming to ambient temperature. The network of cracks may not be sufficient after 1-2 cryocycles to break the material into fragments small enough for a particular reuse application. In this case, additional cryocycles can be carried out in an effort to enhance and refine the cracking. Cryocycling can be continued until the average particle size does not decrease significantly. In general, the numerical values of the key thermomechanical properties that control the effectiveness of cryocycling depend sensitively on the formulation of the explosive or propellant. Interactions between these properties are complex, however, making it difficult to predict the effectiveness of cryocycling for a particular material unless one makes use of the computational tools developed as part of this project.

The thermal and mechanical properties of a material change appreciably during cryocycling. In addition, thermal gradients induced by the temperature changes produce material- and geometry-dependent stresses. Cracks that form quickly during both the freezing and thawing portions of a cryocycle occur because the material's ductility is substantially reduced at low temperature and internal stresses generated by thermally shocking the material exceed local strength. However, since a material's fracture strength often increases with decreasing temperature, there will be an optimum set of conditions that tends to produce the most cracks in the shortest processing time. The net result is that fractures produced during cryocycling depend on a combination of tensile stresses induced by the thermal gradients, stress relief from nearby fractures, and the changing (temperature dependent) material properties.[2]

Advantages of Cryocycling

There are a number of operational advantages associated with cryocycling energetic materials. Although several of these advantages are shared with other technologies, it appears that no other size reduction process offers as comprehensive a list of benefits.

- Cryocycling uses nitrogen, one of the least reactive, least expensive and safest elements known. Because of this, there are no current or anticipated emissions regulations.

11

- Monitoring requirements for the cryocycling process are limited. In effect, only the particle size and nitrogen level must be measured (for personnel safety).

- Tests indicate the detonation sensitivity of energetic materials does not change substantially as a result of the cryocycling process.

- Since liquid nitrogen is non-polar, cryocycling does not alter material composition, and thus this process preserves the inherent energetic content of the material so that it can be reapplied in new products.

- The cryocycling process does not require moving parts, which increases safety and reduces costs.

- Cryocycling induces only the amount of stress required to form cracks and does not add excessive energy to sensitive materials

- There are *no waste streams* if the propellant is reprocessed and reused.

- Cryocycling can easily be combined with other technologies, especially those that benefit from a large increase in surface area and/or small particle sizes.[1-3]

Document Plan

Analysis, development and demonstrations of the cryocycling process were carried out as part of a project under the MOU program on advanced conventional munitions between the Department of Energy and the Department of Defense. The key segments of the project included feasibility studies, stockpile assessment, laboratory studies, and field testing. In particular, numerical models were developed to predict the effectiveness of cryocycling for a given energetic material and to better understand the cryocycling process in general. The modeling effort followed two approaches: 1) analytical modeling using closed form solutions, and 2) numerical modeling using finite element analyses. Analytical models provide a convenient means of classifying candidate materials for cryocycling since they effectively predict the ultimate particle size that can be achieved when a material is cryocycled. The finite element models allow us to simulate the cryocycling process for a variety of propellant compositions and initial geometries. Finite element analyses can therefore be used to address process-critical issues such as optimization, scale-up, and commercialization. The next two sections of the report summarize the analytical and finite element numerical modeling and process simulation results obtained in the project, respectively. The following section summarizes the relevant thermal and mechanical properties of the energetic materials examined in this study. In the fifth section, the DoD stockpile of excess munitions is analyzed to identify those items that are especially suitable for cryocycling. A summary and conclusion of the cryocycling project results is given in the last section.

ANALYTICAL MODELING

Closed-form solutions are used to describe temperature and stress histories induced by cryogenic cycling of slabs of energetic material. These one-dimensional solutions illustrate the role of various material properties and process parameters in determining:

- whether fractures will occur,
- the time required to complete cryocycling,
- the size of fragments obtained from a large chunk on a single cycle,
- the smallest fragment size that can be achieved by repetitive cycling of a material.

Although we focus attention on the simplest case of an infinite slab of thickness 2a, comparative studies have shown that the behavior of spherical masses of diameter 2a is very similar.

Two different levels of analytical modeling are presented. In the first of these, the time-dependent temperature distribution is obtained by summation of a Fourier series. The second approach is based on the presumption of a parabolic temperature profile having a penetration depth, center temperature, and edge temperature which are determined as functions of time. The first approach is mathematically exact and provides verification of the engineering formulas derived by the second, more approximate, approach. In both methods, stress profiles are deduced from the temperature distribution using integral equations derived from the theory of elasticity, taking into account the large change in the elastic modulus that occurs during glass transition.

Comparisons of model predictions with experimental observations are encouraging but underscore the importance of reliable values for the material mechanical properties at cryogenic temperatures.

Governing Equations

The analytical modeling addresses the fundamental problem of fracture initiation and growth in a propellant slab of thickness 2a at an initial temperature T_o that is suddenly plunged into a liquid nitrogen bath at a lower temperature T_b. The temperature distribution within the slab must satisfy the one dimensional conduction equation[4]

$$\rho c \frac{\partial T}{\partial t} = k \frac{\partial^2 T}{\partial x^2} \tag{1}$$

subject to convective boundary conditions of the form[4]

$$-k \frac{\partial T}{\partial x} = h(T - T_b) \qquad \text{at} \qquad x = \pm a \tag{2}$$

The density, ρ, specific heat, c, and thermal conductivity, k, of the solid do not vary greatly with the temperature and, so, are presumed constant.

Since the initial temperature of the slab is much greater than that of liquid nitrogen, the surface of the submerged slab will soon be covered with a film of nitrogen gas. Under these film boiling

conditions, the heat transfer coefficient can be approximated as $h = 1.66 \, \Delta T^{-0.043} \sim$ 140 W/m^{2}K.[5] As cooling proceeds, the temperature difference between the slab surface and the bath, $\Delta T = T_s - T_b$, decreases smoothly until reaching a critical value $\Delta T^* \sim 35 \, {}^oC$ at which the transition from film to nucleate boiling begins to occur. At this point, the heat transfer coefficient increases dramatically, as shown in Figure 1, and as a consequence the temperature difference rapidly falls to a degree or two. The transitional behavior shown in Figure 1 is constructed by smoothly joining the preceding film boiling equation with another expression, $h = 392 \, \Delta T^{3/2}$ [4], based on nucleate boiling data.

During the early film boiling regime, the convective heat transfer coefficient, h, will remain nearly constant at a value of $\sim$140 W/m^{2}K. For this period, the temperature within the slab can be accurately predicted by a well known Fourier series that satisfies Equations (1) and (2) for constant values of the h, k, ρ, c, and T_b.[4]

$$\frac{T - T_b}{T_o - T_b} = \sum_{n=1}^{\infty} \frac{2 \, Bi \, \sec\lambda_n}{Bi \, (1 + Bi) + \lambda_n^2} \; e^{-\lambda_n^2 Fo} \cos(\lambda_n x^*) \tag{3}$$

The dimensionless variables appearing here include the normalized position, Fourier modulus, and Biot number.

$$x^* = \frac{a - x}{a} \qquad\qquad Fo = \frac{\alpha t}{a^2} \qquad\qquad Bi = \frac{ha}{k} \tag{4}$$

Note that the position variables x and x* are measured from the slab surface and the slab center, respectively, and that $\alpha = k/\rho c$ is the thermal diffusivity. The summation of the Fourier series extends over the discrete eigenvalues, λ_n, which are roots of the characteristic equation $\lambda_n \tan\lambda_n = Bi$. Although this solution is not strictly applicable beyond the boiling transition, the abrupt change in surface temperature is small compared to the overall temperature difference, $\Delta T = T_i - T_b \sim 220 \, {}^oC$ so the temperature field will adjust fairly quickly to a reduction in wall temperature from $\sim$110 K to 77 K. We will return to this point in later derivations of closed-form expressions for peak values of thermal stresses.

Virtually all propellants deform elastically at the moderate strains (<1%) and low temperatures of importance to cryocycling. Thus, the theory of elasticity may be used to determine stresses from thermally induced strains [6]. Further, for the case of a submerged slab, the temperature is uniform and the stresses are both uniform and isotropic in the y-z planes that are parallel to the slab faces. This stress, denoted by σ, varies only with x.

$$\sigma(x) = \sigma_{yy} = \sigma_{zz} \tag{5}$$
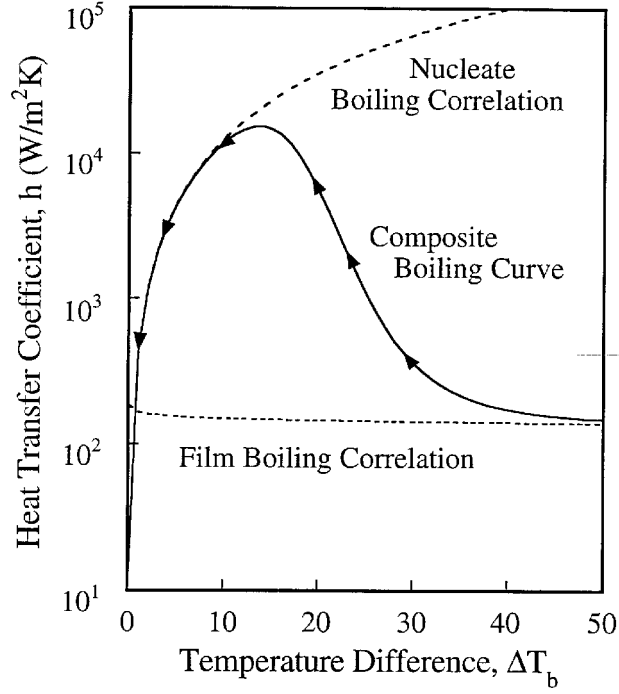
Figure 1. Boiling heat transfer coefficient as a function of temperature difference between cooled surface and liquid nitrogen bath.

All other stress components must vanish, including those acting in the x-direction, provided that no external tractions are applied to the slab faces. The net strain in the y-z plane is the difference between the thermal strain and the opposing stress-related strain.

$$e = e_{yy} = e_{zz} = \int_{T_0}^{T} \beta \, dT + \frac{1-\nu}{E} \sigma \qquad (6)$$

Here, ν is Poisson's ratio, E is Young's modulus, and β is the coefficient of linear thermal expansion. For the materials of interest here, E is strongly dependent on temperature, a factor of central importance to our analysis. We will also take into account the much weaker variations of β with T. Poisson's ratio is assumed to be constant.

The net strain, e, must be constant through the thickness of the slab. This is a direct consequence of the strain compatibility relationships and the symmetry condition at the center of the slab which respectively require that

$$\frac{d^2 e}{dx^2} = 0 \qquad \text{and} \qquad \frac{de}{dx} = 0 \qquad (7)$$

Thus, by a rearrangement of Equation (6), the stress at any point in the solid is given by

$$\sigma(x) = -\phi[T(x)] + \frac{e}{1-\nu} E[T(x)] \quad \text{where} \quad \phi = \frac{E}{1-\nu} \int_{T_0}^{T} \beta \, dT \qquad (8)$$

15

and the constant strain e is determined by the requirement that there be no net force on any y-z plane through the slab.

$$\int_{-a}^{a} \sigma \, dx = -\int_{-a}^{a} \phi \, dT + e \int_{-a}^{a} \frac{E}{1-\nu} \, dx = 0 \tag{9}$$

The final expression for the stress field may then be written as

$$\sigma(x) = -\phi + \frac{E}{\overline{\overline{E}}} \, \overline{\phi} \tag{10}$$

where

$$\overline{\phi} = \frac{1}{2a} \int_{-a}^{a} \phi \, dx \qquad \text{and} \qquad \overline{\overline{E}} = \frac{1}{2a} \int_{-a}^{a} E \, dx \tag{11}$$

In these equations, both ϕ and E are functions of temperature and, hence, position.

When the mechanical properties are constant, Equations (10) and (11) reduce to the well known formula[6]

$$\sigma = -\frac{\beta E}{1-\nu} (T - \overline{T}) \tag{12}$$

which relates the local stress to the difference between local and mean temperatures within the slab. Thus, when the slab temperature is uniform, at either the ambient temperature or the bath temperature, there can be no thermal stress. The same is true of the earlier equations that include the effects of a temperature dependent modulus. Further, since the slab surface temperature may decrease to nearly the bath temperature, T_b, without changing the mean temperature, T_0, of a very thick slab, the maximum attainable thermal stress is

$$\sigma_0 = -\frac{\beta E}{1-\nu}(T_b - T_0) \qquad \text{or} \qquad \sigma_0 = -\frac{E(T_b)}{1-\nu} \int_{T_0}^{T_b} \beta \, dT \tag{13}$$

for the respective cases in which properties are constant or temperature dependent. These maximum values are used to normalize the stresses appearing later in several plots.

The energetic materials of interest undergo a structural transition within a fairly narrow temperature range centered about the so-called glass transition temperature, Tg. As seen in Figures 32 and 34 in the section on Thermal and Mechanical Properties of Solid Propellants, the elastic modulus and yield strength typically increase by two or three orders of magnitude in passing from a compliant "rubber" state with T > Tg to a "glass" state with T < Tg. In the rubber state the material has greater segmental mobility and is therefore much more compliant than it is in the glassy state [7]. Thus, thermal stresses will remain very small when cooling from room temperature down to Tg. At that point, the prior thermal strain will be locked in by the transition. Further cooling below Tg will then induce incremental strains which are resisted by the much

16

stiffer glassy material. For this reason, it is appropriate to break the thermal expansion integral, ϕ, into two components which are evaluated separately for temperatures above and below Tg.

$$\phi(T) = \frac{E(T_{g+})}{1-\nu} \int_{T_0}^{T_g} \beta dT + \frac{E(T)}{1-\nu} \int_{T_g}^{T} \beta \, dT \tag{14}$$

A failure to split the integral in this manner would imply that the stress in the material suddenly increases by three orders of magnitude during transition, in conflict with physical expectations.

Fortunately, since the glass transition is fairly abrupt and the stresses are small prior to transition, there is little need to develop a detailed thermodynamically consistent model of the constitutive behavior before and during glass transition. It is only important to correctly account for the stresses and strains that occur at temperatures below Tg. In that temperature range, $T_g > T > T_b$, the modulus typically varies by no more than a factor of three.

Fourier Series Solutions

Time histories of T and σ are generated by evaluating the foregoing equations for sequential choices of the Fourier number, Fo. The Biot number is first determined for particular values of k, a, and the convective heat transfer coefficient, h, determined from the boiling correlation shown earlier in Figure 1. Once Bi has been established, the temperature profile $T(x_i)$ is calculated by summing the series solution at a discrete set of points x_i. The corresponding stress profiles $\sigma(x_i)$ are next generated, by trapezoidal integration of Equations (10) and (11) using the temperature dependent property variations shown in the section on Thermal and Mechanical Properties of Solid Propellants (Figures 32 and 34).

A typical family of temperature profiles is shown in Figure 2 for a 50 mm slab of CYH. At Fo = 10^{-2} the slab surface temperature has just fallen below the glass transition temperature of 225 K. Thereafter, in the time window between Fo = 3×10^{-2} and 10^{-1}, the transition from film to nucleate boiling occurs, causing a considerable increase in the heat transfer coefficient and a corresponding reduction of the surface temperature. By Fo = 1, the slab is nearly equilibrated with the liquid nitrogen bath.
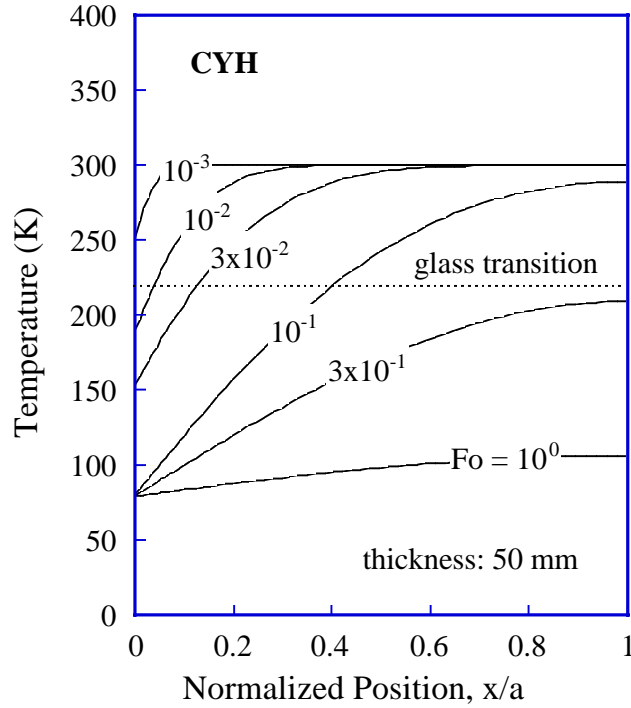
Figure 2. Predicted temperature profiles in a 50 mm slab of CYH.

The corresponding stress distributions presented in Figure 3 are strongly influenced by the thousand-fold increase in elastic modulus which occurs as the material passes through its glass transition at 225 K. Prior to $Fo = 10^{-2}$, nearly all of the material remains warmer than the transition temperature, T_g. For that time, the stiffness of the warm propellant is so small that thermally induced stresses remain negligible. As cooling proceeds beyond $Fo = 10^{-2}$, the glass transition front sweeps inward from the surface to the interior. By $Fo = 10^{-1}$, the outer 40% of the slab has been cooled below T_g, as apparent in the stress profiles which indicate significant stresses over the interval $0 < x/a < 0.4$. In that stress profile and all of those for later times, it is apparent that surface tensile stresses are balanced by internal compressive stresses, and that this balance must be struck within the high-modulus material. This restriction of stresses to the thermally influenced region reduces the maximum tensile stresses to less than 1/4 of the maximum attainable stress, σ_0 of Equation (13), which is used as a reference stress in scaling the vertical axis of Figure 3.

Figure 3 illustrates two important aspects of cryocycling that are generally valid regardless of process parameters. First, it is seen that the maximum stress occurs in a time range from $Fo = 0.1$ to 0.3, a time much shorter than the thermal equilibration time of $Fo = 1.0$.
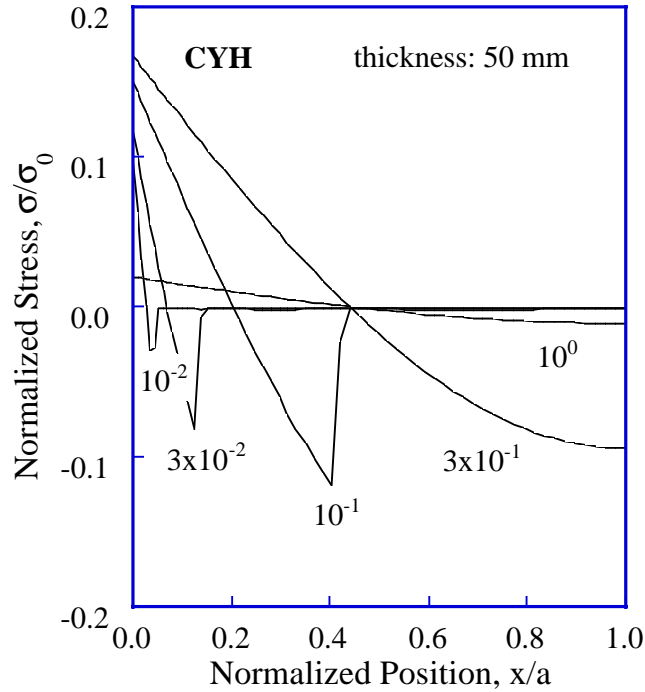
Figure 3. Predicted stress profiles in a 50 mm slab of CYH.

Cooling beyond Fo = 0.3 thus provides no added benefit and needlessly extends both the cooling and warming phases of the cycle. The second general observation is that the stress always remains compressive in the central region of the slab indicating that the fractures produced on cooling cannot penetrate more than about 50% to 70% of the distance from the surface to the center. It is, however, possible to extend fractures through the center of the slab by subsequently heating the exterior, thereby producing compressive stresses at the surface and tensile stresses in the interior. Accordingly, sequential cycles of rapid cooling and heating should be particularly effective in breaking a material.

The occurrence of fracturing can be predicted by comparing the local time-dependent stress at the surface with the temperature-dependent, and hence time-dependent, strength which applies at the same location. As the slab surface temperature drops, material adjacent to the surface undergoes the glass transition and the strength of this material typically increases by about one order of magnitude. This occurs before significant stresses build in the slab. As cooling continues, and more of the slab undergoes the glass transition, the stresses begin to build. Thereafter, the ratio of stress to strength grows for a while, reaches a maximum, and then subsides as temperatures equilibrate and stresses finally diminish.

Figure 4 displays the calculated maximum ratio of stress to strength for five propellants, two propellant simulants (LWCYH and H19), and the polystyrene which was used in cryocycling experiments. The order from left to right is based on the experimental ranking of "best" to "worst" susceptibility to cryocycling. CYH is the only exception to this horizontal ranking. Since it has not yet been subjected to cryocycling experiments, it was placed between the two most similar materials, EJC and LWCYH. The calculated ratio of stress to strength is clearly greatest at the left, falling gradually to the right, in keeping with the experimental ranking. The ratio of

stress to strength is greater than unity for all materials (except H19), indicating that a 25 mm slab of any one (except H19) should fracture.
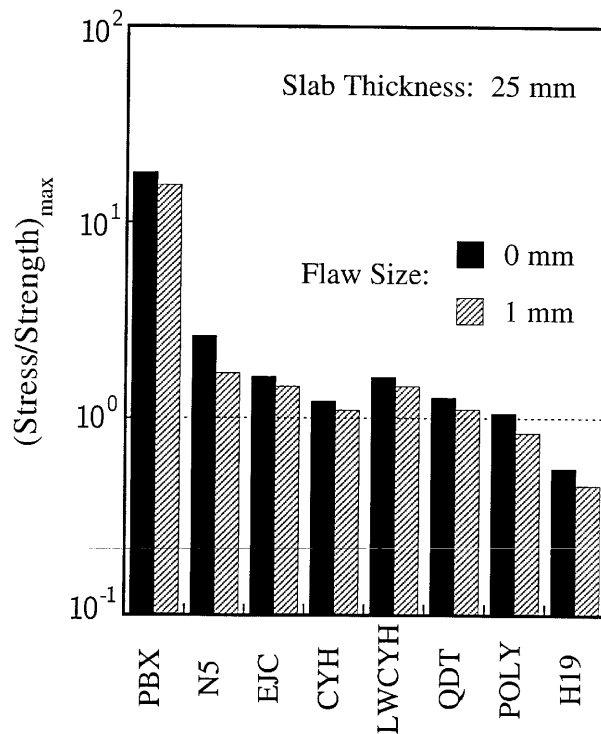
Figure 4. Maximum ratio of stress to strength; comparison of predictions (bar height) with experimental observations (horizontal ranking).

The minimum fragment size obtainable by cryocycling can be estimated by calculating the maximum ratio of stress to strength for successively smaller slab thicknesses. As the thickness decreases, heat conduction becomes more effective in reducing the temperature difference and thermal stress within the slab. The minimum fragment sizes shown in Figure 5 are the slab thicknesses for which the ratio of stress to strength is unity. Presumably a slightly thicker slab would fracture, while a slightly thinner slab would remain intact. As such, there is an inherent uncertainty of about a factor of two in the calculated minimum fragment size. Note the smallest sizes are predicted for the leftmost materials that were, in fact, deemed "best" in cryocycling experiments because they yielded the smallest fragment sizes.

The predicted fragment sizes shown in Figure 5 agree reasonably well with those observed experimentally. For example, cryocycling of H19 resulted in an average particle size of 60 mm, in remarkable agreement with predictions. In the middle of the spectrum, LWCYH broke down to an average particle size of roughly 8 mm, as compared with a prediction of 6 mm; QDT and EJC produced similar particle sizes, in general agreement with the model. Cryocycling of PBX produced many small fragments (<5 mm) which were themselves severely cracked and so friable that the ultimate particle size was expected to be less than 1 mm. Indeed, the predictions suggest that a considerably smaller size (0.2 mm) would be obtained if the material behaved as a continuum at length scales of less than 1 mm.
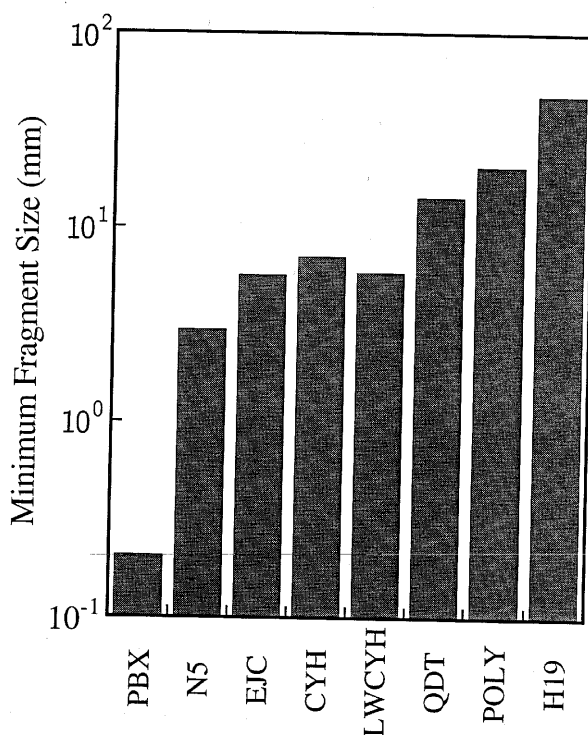
Figure 5. Minimum particle size obtainable by cryofracture; comparison of predictions (bar height) with experimental observations (horizontal ranking).

While these comparisons of analytical and experimental results are generally encouraging, they nevertheless illustrate the importance of obtaining reliable measurements of strength and modulus, especially at the liquid nitrogen temperature. For example, a 50% uncertainty in either of these quantities can result in an and order of magnitude uncertainty in predicting the ultimate particle size, since the maximum attainable stress rarely exceeds the cryogenic strength by more than 50% to 100%. Among the materials considered here, polystyrene and PBX are probably the best characterized, since they experience glass transition above or near room temperature. The properties of QDT and EJC have been carefully measured by Hercules at liquid nitrogen temperature but are lacking at intermediate temperatures. Conversely, the temperature dependence is known for CYH and N5 from 173 to 300 K, but the very low temperature behavior must be extrapolated. Finally, although the properties of the inert propellant simulants, LWCYH and H19, were measured over the full temperature range, the two different experimental techniques used in these measurements produced different values for the low temperature modulus; we chose to use the larger values for the sake of consistency with other materials.

Derivation of Engineering Formulas

Although the preceding analysis has been analytical rather than numerical, the solutions involve series summations and integrations that are best performed by a computer program having hundreds of executable statements. It would clearly be preferable if predictions of peak stresses and fragment sizes could be made using engineering formulas that were readily evaluated using a hand calculator or a simple spread sheet program. To meet this need, we have derived approximate solutions to the governing equations and evaluated their accuracy by comparison with the exact solutions given earlier.

In developing these approximate solutions we first consider the simplest case in which the mechanical properties and boiling heat transfer coefficient are constant. The approximate solutions are then extended to include the effects of both the glass transition and the boiling transition.

The temperature distribution, $T(x,t)$, across a convectively cooled slab can be well approximated by a function of the form

$$\frac{T - T_c}{T_s - T_c} = \xi^m \qquad \text{where} \qquad \xi = \frac{\delta - x}{\delta} \qquad (15)$$

Here, $T_s(t)$ and $T_c(t)$ are the time-dependent temperatures at the surface and center, respectively; $\delta(t)$ is the penetration depth of the thermal disturbance, x is measured from the slab surface, and ξ is the normalized distance measured backwards from the leading edge of the thermal front.. The power, m, should be greater than unity in order that there be no heat flow ahead of the disturbance when $\delta < a$ and no heat flow across the center plane when $\delta = a$. We will later set $m = 2$ to obtain a parabolic profile but will first show that results are relatively insensitive to reasonable choices of this parameter. Substitution of this temperature profile into the convective boundary condition, Equation (2), yields the following expression for the ratio of the internal temperature difference within the solid, ΔT_s, to the external temperature difference within the bath, ΔT_b.

$$\frac{\Delta T_s}{\Delta T_b} = \frac{T_c - T_s}{T_s - T_b} = \frac{Bi\delta^*}{m} \qquad \text{where} \qquad \delta^* = \frac{\delta}{a} \qquad (16)$$

For later convenience it is also useful to write expressions for ΔT_s and ΔT_b in terms of the overall temperature difference between the slab center and the bath $\Delta T = \Delta T_s + \Delta T_b$.

$$\frac{\Delta T_s}{\Delta T} = \frac{Bi\,\delta^*}{m + Bi\,\delta^*} \qquad \text{and} \quad \frac{\Delta T_b}{\Delta T} = \frac{m}{m + Bi\,\delta^*} \qquad (17)$$

In subsequent stress analysis, the overall temperature difference, ΔT, between the slab center and the bath will be varied to identify the condition of maximum stress.

The stresses within the slab are next determined by substitution of the analytical temperature profile into the integral Equations (10) and (11). The peak stress can then be written in terms of the penetration depth δ and the temperature difference across the solid, ΔT_s. To identify the peak stress, we first consider the initial phase of cooling when the penetration depth, δ, varies from 0 to a, while the center temperature remains fixed at its initial value, T_0. At later times δ is equal to a, while the center temperature is decreases from T_0 to T_b. During both periods, Equation (17) is used to determine the temperature drop across the slab, ΔT_s, for the known or selected values of the overall ΔT. The maximum stress is identified either by inspection or by differentiation with respect to the parameters δ or ΔT, taking into account the point at which boiling transition occurs.

To illustrate the use of this approach, let us first consider the case in which all of the physical properties and the heat transfer coefficient, h, are constant. Substitution of the presumed temperature profile into the thermal expansion integrals, Equations (8) and (11), yields

$$\phi = \frac{-E\beta}{1-\nu}\left[\Delta T_s\ \xi^m + (T_c - T_0)\right] \qquad \text{and} \qquad \bar{\phi} = \frac{-E\beta}{1-\nu}\left[\frac{\Delta T_s}{m+1}\ \delta^* + (T_c - T_0)\right] \qquad (18)$$

When E is uniform, the stress at the surface is simply the difference between these quantities.

$$\sigma(a,t) = -\phi_{(\xi=1)} + \frac{E}{\overline{E}}\bar{\phi} = \frac{E\beta\Delta T_s}{1-\nu}\left[1 - \frac{\delta^*}{m+1}\right] = \frac{E\beta\Delta T}{1-\nu}\left(\frac{Bi\ \delta^*}{m + Bi\ \delta^*}\right)\left[1 - \frac{\delta^*}{m+1}\right] \qquad (19)$$

At early times, the overall temperature difference is fixed at $\Delta T = T_0 - T_b$ and the surface stress is a function of δ^* alone. By differentiating this function with respect to δ^* and equating the result to zero we obtain the following expression for the penetration depth corresponding to the maximum stress.

$$\delta^* = \frac{m}{Bi}\left[-1 + \sqrt{1 + Bi\frac{m+1}{m}}\right] \qquad (20)$$

This value of δ^* is then substituted into the preceding equation to obtain the maximum value of the surface stress.

Figure 6 compares the peak stresses predicted by the above formulas (solid lines) with those calculated by the exact Fourier series analysis (symbols). The three solid lines indicate results obtained for presumed temperature profiles which are linear (m = 1), quadratic (m = 2), and cubic (m = 3). The good agreement among these three results suggests a desirable insensitivity to assumptions, though the parabolic profile generally provides the best match to exact results and is used in subsequent plots. The peak stress is greatest when the Biot number is large, because the surface temperature in these cases decreases to bath temperature long before the center temperature, resulting in a large difference between the surface and the mean temperatures. Hence, there is a large difference in thermal strain and a large stress, in accordance with Equation (12).

23
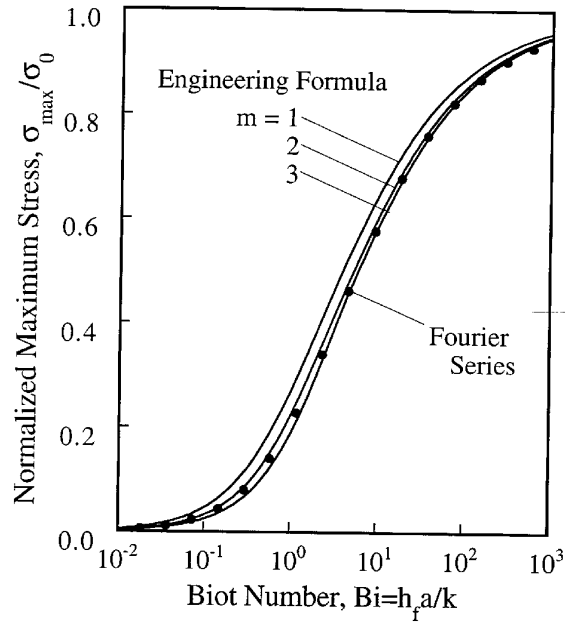
Figure 6. Maximum stress for convective cooling of slabs having constant mechanical properties.

The timing and magnitude of the maximum stress are significantly altered by the change in material properties that occur during glass transition. In the absence of this transition, the properties are relatively constant and the maximum surface stress occurs either before or at the time of the arrival of the thermal front at the slab center, as predicted by Equation (20). It can be seen by inspection of Equation (19) that, when properties are constant, the stress must decrease at later times, since δ^* is then fixed at unity while the overall temperature difference, ΔT, decreases with continued cooling. However, when a glass transition occurs during cooling, the maximum stress is generally delayed until after a substantial fraction of the slab has cooled below the glass transition temperature, T_g. Prior to that time the portion of the interior that is warmer than T_g will have a small modulus and cannot resist the contraction of the cooler surface material.

Since the glass transition usually occurs over a relatively narrow temperature range, we will assume that the elastic modulus undergoes a step change at a distinct temperature, T_g, but is constant on each side of the transition.

$$E = E_g, T \leq T_g \qquad E = E_r, T > T_g \qquad E_g \gg E_r \qquad (21)$$

Further, since the modulus in the glass state, E_g, exceeds that in the rubber state, E_r, by two or three orders of magnitude, the stress in the low modulus material may be safely neglected. Finally, the thermal expansion coefficient will be assigned a constant value, β_g, that represents the average over the low temperature range from T_g to T_b. Under these simplifications, the assumption of a parabolic temperature profile, and the condition that $\delta^* = 1$, the stress integrals in Equations (8) through (11) yield the following expression for the stress at the surface.

24

$$\sigma(a, t) = \frac{E_g \beta_g}{1 - \nu}\left(T_g - T_b\right)\left[\frac{B}{1 - B x_g^{*2}}\right]\left(1 - \frac{1}{3}\frac{1 - x_g^{*2}}{1 - x_g^{*3}}\right) \qquad \text{where} \qquad x_g^* = \frac{x_g}{a} \qquad (22)$$

Here, $x_g^*(t)$ is the normalized position of the glass transition point, measured from the slab center, and $B = Bi/(2+Bi)$. When this function is plotted versus x_g^*, it is found that the surface stress increases monotonically as the glass transition sweeps through the material from the surface where $x_g^* = 0$ to the center where $x_g^* = 1$. Beyond that time, the stress declines with the decreasing temperature difference.

Having established that the maximum stress occurs just as the glass transition front reaches the slab center, the corresponding magnitude of the stress is given by Equation (22) evaluated at $x_g^* = 0$.

$$\sigma_{max} = \frac{2}{3}\frac{E_g \beta_g}{1 - \nu}\left(T_g - T_b\right)\left(\frac{Bi}{2 + Bi}\right) \qquad (23)$$

Figure 7 shows a comparison between this formula (solid lines) and exact solutions (symbols) for several values of a parameter indicating the fraction of the overall temperature drop that remains when glass transition front has just reached the center and, hence $_c \pm T_g$.

$$\Delta T_g^* = \frac{T_g - T_b}{T_0 - T_b}$$

(24)

The exact solutions use temperatures profiles generated from the Fourier series; the corresponding stresses are based upon a constant β_g and a modulus that abruptly increases from E_r to E_g at the glass transition temperature, T_g. Thus, the formula is in good agreement with exact results when both methods use the same property data. Although the engineering formula is based on the assumption that $E_r/E_g \ll 1$, this should be easily satisfied by the propellants of interest which typically have a modulus ratio, E_r/E_g, of 10^{-3}. That value was used in constructing the exact solutions of Figure 7.

It is important to know whether the boiling transition occurs before the glass transition front reaches the slab center. If so, a very large, essentially infinite, value of h should be used to calculate the Biot number appearing in the formula (23) for the maximum stress. As mentioned earlier, the boiling transition typically occurs when the temperature difference between the wall and the liquid nitrogen is around 35 $^{\circ}$C. This can be seen in Figure 8 which shows the surface temperature history for slabs having half-thicknesses, a, of 1, 10, 100, and 1000 mm. These
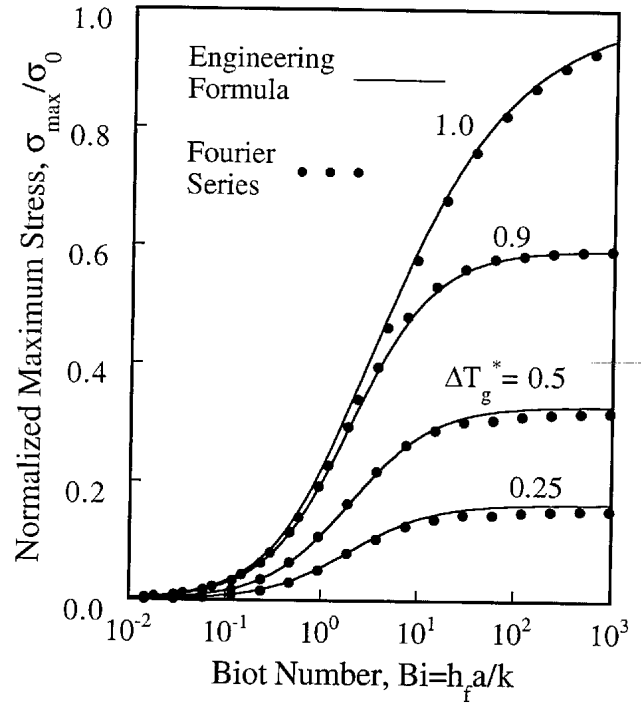
Figure 7. Maximum stress for convective cooling of slabs having a glass transition at various temperatures between the initial and bath temperatures.
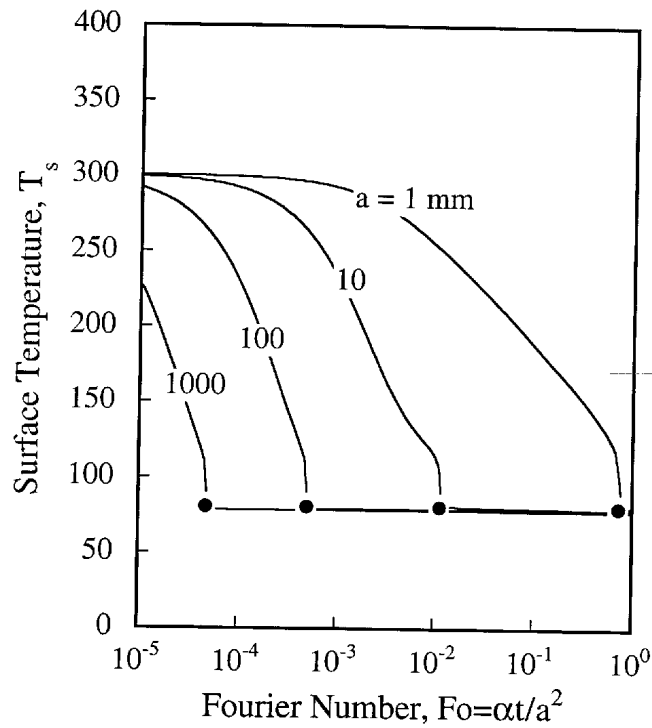
Figure 8. Surface temperature histories showing boiling transition at a point where the surface temperature is roughly 35°C greater than the bath temperature.

26

solutions were calculated using a time-marching finite-difference method. The time integration was performed using a stiff ordinary differential equation solver that automatically adjusts the time step to accurately predict the temperature profiles, even when the heat transfer coefficient is changing very rapidly. This alternative method of solution was used primarily to investigate the boiling transition, but it also serves as a check of both the Fourier series solutions given earlier and the engineering formulas derived here.

Having concluded that the boiling transition occurs for a critical temperature difference, $\Delta T_b{}^*$, of roughly 35 $^\circ$C, the corresponding value of the slab center temperature, $T_c{}^*$, can be estimated from the following rearrangement of Equation (17).

$$T_c^* = T_b + \left(\frac{2 + Bi}{2}\right)\Delta T_b^* \qquad \text{where} \qquad \Delta T_b^* \approx 35^\circ C \qquad (25)$$

Since the boiling transition does not occur until after the center has cooled to this temperature, the Biot number appearing here should be evaluated using the heat transfer coefficient for film boiling ($h_f \sim 140$ W/m^{2}K). The bath temperature, T_b, is simply a constant. So, $T_c{}^*$ depends only on $Bi = h_f a/k$. Further, since $T_c{}^*$ increases with Bi, and hence increases with a; thick slabs will have $T_c{}^* > T_g$.

If $T_c{}^* > T_g$, the boiling transition occurs prior to completion of the glass transition, indicating that h, and hence Bi, will be extremely large when the glass transition front later arrives at the slab center. Under these circumstances, Equation (23) reduces to

$$\sigma_{max} = \frac{2}{3}\frac{E_g \beta_g}{1-\nu}\left(T_g - T_b\right) \qquad \text{for} \qquad T_c^* > T_g \qquad (26)$$

This is equivalent to assuming that the surface temperature of the slab is the same as the bath temperature after the boiling transition has occurred, in keeping with the temperature histories. of the preceding Figure 8. Conversely, if $T_c{}^* < T_g$, the film boiling coefficient, h_f, should be used to calculate the Biot number appearing in the more general Equation (23) for the maximum stress.

Figure 9 compares the peak stresses calculated by the above formulas with those predicted by the more exact methods. All three methods are in good agreement, particularly considering the simplicity of the approximate formulas. The only significant differences among solutions occur in the immediate vicinity of the boiling transition. The behavior in this region would be somewhat uncertain in any case, since the details of the boiling transition shown in Figure 1 are not accurately known. Thus, the overall accuracy of the predictions is hardly diminished by using the approximate formulas.

The influence of the boiling transition is clearly apparent in Figure 9. A sharp rise in peak stress occurs in the region where the boiling transition occurs just as the glass transition is completed. The Biot number corresponding to this condition can be found by equating $T_c{}^*$ to Tg in equation (25) and then solving for the critical value of Bi.

$$\mathrm{Bi_{crit}} = 2\left[\frac{T_g - T_b}{\Delta T_b^*} - 1\right] = 2\left[\Delta T_g^* \frac{T_0 - T_b}{\Delta T_b^*} - 1\right] \approx 8 \qquad (27)$$
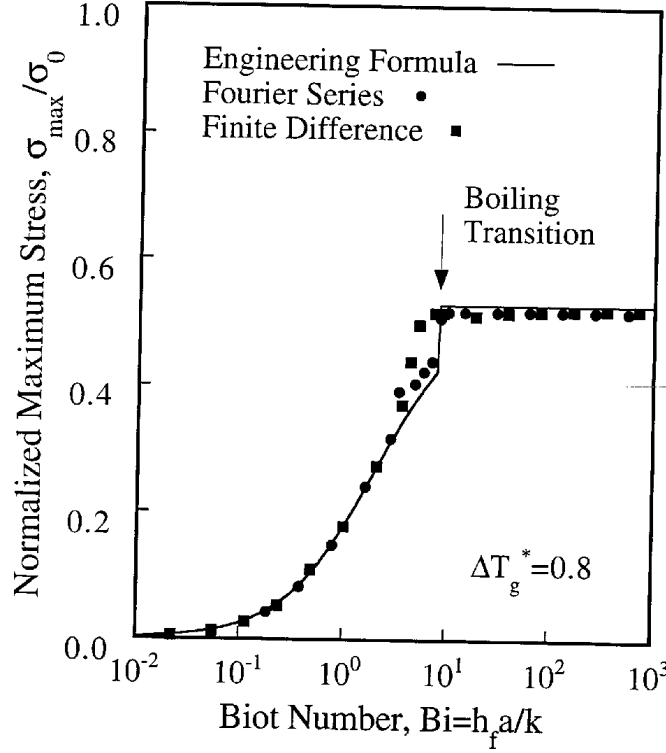
Figure 9. Maximum stress for cooling of a slab by boiling heat transfer, including effects of boiling transition and glass transition.

The corresponding slab half-thickness follows immediately from the definition of the Biot number.

$$a_{crit} = \mathrm{Bi_{crit}} \frac{k}{h_f} \approx 10\,mm \qquad (28)$$

The numerical values indicated in the last two equations correspond to the typical parameters used in constructing Figure 9 ($T_g^* = 0.8$, $T_0 = 300$ K, $T_b = 77$K, $\Delta T_b^* = 35$K, $k = 0.2$, w/mK). For values of Bi or slab thickness greater than the critical values, the heat transfer coefficient will be very large, and hence the surface temperature will be very low. The overall temperature difference will then be very large when the glass transition front reaches the slab center. These conditions will produce the maximum possible surface stress, that given by Equation (26).

For slabs thinner than the critical thickness, a_{crit}, peak stresses will be reduced in accordance with Equation (23). This equation may also be used to discern the minimum attainable fragment size by first setting σ_{max} to the cryogenic strength σ_u, then solving for the corresponding Bi, and finally converting that Bi to a minimum fragment size. The results is

$$a_{min} = \frac{k}{h_f}\left[\frac{2}{f-1}\right] \quad \text{where} \quad f = \frac{\sigma_{Bi\to\infty}}{\sigma_u} = \frac{1}{\sigma_u}\left[\frac{2}{3}\frac{E_g\,\beta_g}{1-\nu}\left(T_g - T_b\right)\right] \quad (29)$$

The ratio f must, of course, be greater than unity if fragmentation is to occur for slabs of any thickness.

When the thickness of a propellant slab is greater than the minimum thickness, a_{min}, tensile fractures will initiate at the surface and propagate toward the slab center. The stress intensity at the fracture tip will initially increase as the fracture grows longer, resulting in rapid unstable propagation through the region which is subjected to tensile stresses. As these tensile stresses are relieved, the balancing compressive stresses in the slab center will also be reduced, allowing the fracture to reach almost to the center of the slab.

The formation of a fracture relieves tensile stresses in adjacent material, preventing subsequent initiation of additional fractures in the immediate vicinity. The range of this stress relief can be judged from the following relationship which represents the far field behavior of the exact solution for the stress field surrounding a wedge shaped fracture in an infinite medium[8]

$$\frac{\sigma}{\sigma_\infty} = \left[\frac{y/L}{\sqrt{1+(y/L)^2}}\right]^3 \quad (30)$$

This equation describes the magnitude of the local tensile stress, σ, relative to the undisturbed tensile stress , σ_{inf} , that existed everywhere on the slab face prior to the fracture initiation. That maximum stress still persists on portions of the slab face that are sufficiently far from the fracture. The fractional stress still remaining at closer ranges depends on the distance, y, measured from the fracture (perpendicular to its surface expression) along the surface of the slab. The distance is, of course, scaled by the "length" of the fracture, L, which, in our case is the depth of its penetration into the slab, roughly equal to the half thickness, a. This approximate relationship, given by Equation (30), is plotted as a solid line in Figure 10, along with the corresponding exact results tabulated by Lachenbruch[9]. The agreement is more than adequate for present purposes.

The plot shows Normalized Stress, σ/σ_{max} (y-axis, 0.0 to 1.0) versus Normalized Position, y/L (x-axis, 0 to 5).

$$\frac{\sigma}{\sigma_\infty} = \left[\frac{y/L}{\sqrt{1+(y/L)^2}}\right]^3$$

— Approximate Formula

• Exact Solution
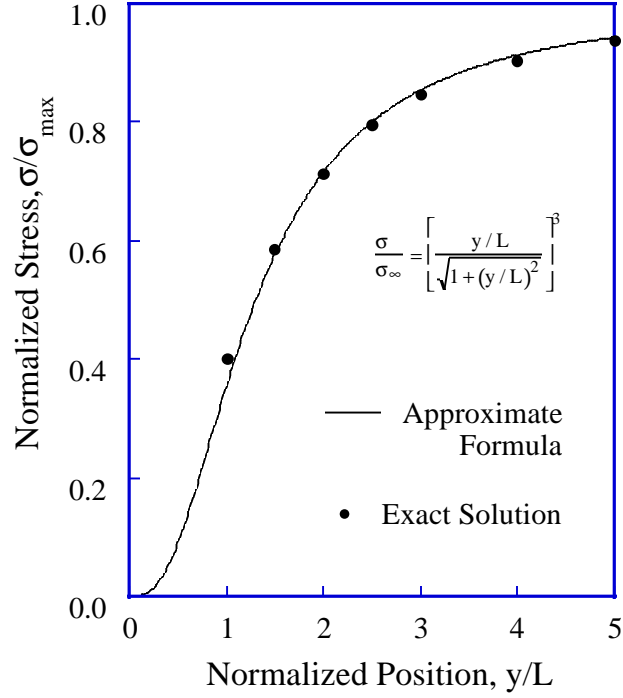
Figure 10. Variation of stress with distance from a fracture having penetration depth L.

To determine the approximate spacing, s, between parallel fractures produced in a single thermal cycle, it is only necessary to invert Equation (30) so that it expresses the distance, s = y, from a first formed fracture at which the remaining tensile stress is equal to the cryogenic strength σ_u. In doing so, L is equated to a, since first formed fractures are expected to approach the slab center, and σ_{inf} is equated to σ_{max}.

$$\frac{s}{a} = \sqrt{\frac{1}{R^{2/3} - 1}} \qquad \text{where} \qquad R = \frac{\sigma_{max}}{\sigma_u} \qquad (31)$$

Here again, R must be greater than unity. It is similar to the ratio f defined previously in Equation (29) except that R now includes the effect of the Biot number that appears in Equation (23), the defining equation for σ_{max}. R is precisely the quantity which was plotted earlier in Figure 4 for a number of propellants.

Figure 11 illustrates the dependence of relative fracture spacing, s/a, on the ratio of maximum thermal stress to cryogenic strength, R.. Both s/a and s/2a are shown, since the latter indicates the fracture spacing relative to the total thickness of the slab. We see that a maximum stress which is 40% greater than the strength (ie. R = 1.4) would break the slab into cubes having an edge length equal to the initial slab thickness (ie. s/(2a) = 1). This stress ratio is typical of the propellants included in Figure 4, as are the corresponding fragment sizes. We further see in
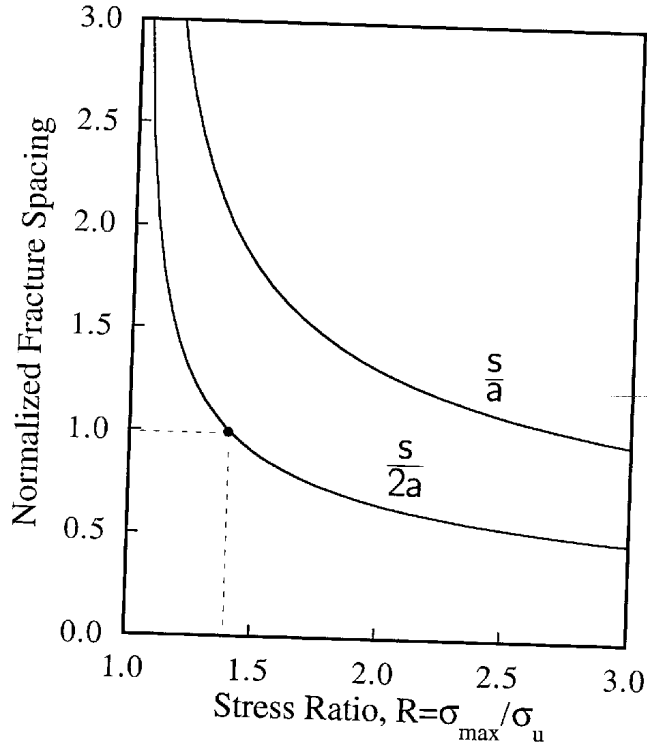
Figure 11. Minimum spacing between parallel fractures as a function of ratio between maximum surface stress and cryogenic strength.

Figure 11 that very large stresses would be required to produce small fragments on a single cycle, but that very moderate stress excesses, as small as 10 to 15%, are sufficient to produce fragments having dimensions no more than twice the initial slab thickness. Thus, even moderate stress excesses may be sufficient for successful cryocycling.

If the relative fracture spacing predicted by Equation (31) is less than unity, it is likely that some of the fractures will arrest long before reaching the slab center. The competition among growing parallel fractures usually requires that their depth be no greater than their spacing. Thus, if the spacing at the surface were s = a/4, roughly half of the fracture would arrest at a length of a/4 and the other half would continue to grow toward the slab center. Each of the short fractures would lie between a pair of longer ones. A stability analysis that predicts this behavior has been developed in the context of heat extraction from geothermal reservoirs[10].

The engineering formulas derived here may be used in a sequential fashion to predict the outcome of a proposed cryofracture process based on known values of k, α, h_f, a, β_g, E_g, T_g, T_o, T_b, and ΔT_b, σ_u. The following outline of this procedure will serve as a summary of the main results.

31

- Required cooling time:

$$t = 0.2\left(\frac{a^2}{\alpha}\right)$$

- Critical material thickness needed to realize maximum possible tensile stress:

$$a_{crit} = 2\frac{k}{h_f}\left[\frac{T_g - T_b}{\Delta T_b^*} - 1\right]$$

- Peak tensile stress at the cooled surface (use $Bi = h_f a/k$ for $a < a_{crit}$, $Bi =$ infinity for $a > a_{crit}$):

$$\sigma_{max} = \frac{2}{3}\frac{E_g\beta_g}{1-\nu}(T_g - T_b)\left(\frac{Bi}{2+Bi}\right)$$

- Occurrence of fracture:

$$R = \frac{\sigma_{max}}{\sigma_u} > 1$$

- Fracture spacing produced by a single thermal cycle:

$$s = \frac{a}{\sqrt{R^{2/3} - 1}}$$

- Minimum attainable fragment size for multiple cycles:

$$a_{min} = \frac{k}{h_f}\left[\frac{2}{f-1}\right] \quad \text{where} \quad f = \frac{1}{\sigma_u}\left[\frac{2}{3}\frac{E_g\beta_g}{1-\nu}(T_g - T_b)\right]$$

These formulas may be applied to situations in which no glass transition occurs during cooling by simply equating T_g to T_0.

FINITE ELEMENT CRYOCYCLING SIMULATION

Goals and Objectives of Finite Element Analysis

The primary goal of the finite element analyses was to predict the thermo-structural response of rocket motor propellants and explosives during the first cryocycle. In this way, we can better understand the process and investigate the conditions that most effectively cause cracking during both liquid nitrogen immersion and warm-up. The analytical process does not allow for removal of cracked material (elements) in order to expose underlying propellant to further cooling or warm-up, therefore carrying the analyses too far past initial cracking would not be meaningful.

The initial step required for the thermo-structural predictions was the development of a technique for the analysis of the response of the energetic materials in the first cryocycle, including the warm-up phase. Once a method was developed, individual grain geometries for particular rocket motors were modeled and analyzed. The finite element analyses were also used to study the process of cracking in case-bonded grains compared to those which could be cryocycled without the case.

Choice Of Finite Element Codes

The choice of the finite element code(s) for the cryocycling program was driven by several requirements. The criteria considered are summarized below.

1) Predict the initiation of structural cracks.
2) Predict crack growth.
3) Can perform thermal analyses with time dependent thermal material properties.
4) Can perform structural analyses with time dependent structural material properties.
5) Non-linear stress/strain behavior.
6) Straightforward coupling between thermal and structural analyses.
7) Use existing code capabilities wherever possible. Minimize the need for capability development, but consider easy to implement extensions.

The codes considered for this study were those that are widely used at Sandia for thermal and structural analysis. These include PRONTO[11], JAC2D[12], JAC3D[13], COYOTE II[14,15], JACQ[16], and ABAQUS[17]. All the above criteria could not be met with these codes at the initiation of the study. Since all these codes are under continual development, reexamination of their use was made during the study. Though improvements were made in capabilities during this period, we found that no code could meet all requirements even at the conclusion of the study.

The PRONTO code uses an explicit time integrator which is appropriate for problems which have extremely high strain rates. The explicit time integrator forces the time step to be less than the time it takes for a dilational wave can traverse the smallest element. In quasi-static problems this is problematic since the times of interest are long. This situation can be averted in some cases by introducing a fictitiously high material density (and thus lowering the dilational wave speed). This same problem exists with the explicit time integrator version of ABAQUS. Also, PRONTO does not have a documented thermoelastic capability, though modifications can be performed which involve reading a temperature file, and using it in a thermoelastic analysis. Reference 18 shows how this modification to PRONTO can be tailored to the design of fast burst nuclear reactors.

JAC2D and JAC3D are programs that solve large deformation, temperature dependent quasi-static mechanics problems in two and three dimensions, respectively. The JAS3D code[19] is the successor to the JAC series of codes. The JAC codes use a nonlinear conjugate gradient technique to solve the governing nonlinear equations. JAS3D can be thermally driven in one of two ways. The first is in a manner which is tightly coupled to the thermal mechanics code, COYOTE II. Thermal and structural data are exchanged once per time step. This capability was developed[20] subsequent to the beginning of the cryocycling program and is presently being evaluated at

Sandia. The second way of transferring data from a thermal code to JAS3D would be through the exercise of another code MERLIN II[21]. The MERLIN II program is designed to transfer data between finite element meshes of arbitrary geometry. The thermal code would run first. Most likely this would be COYOTE or JACQ. JACQ is another thermal code written at Sandia. Damage can be simulated in JAS3D via the Sandia damage model.[22] However, this damage model is only appropriate for ductile materials. When cracking occurs (low temperatures) during cryocycling, the materials of interest are essentially brittle.

All of the codes discussed above were developed at Sandia and are supported by various Sandia organizations. ABAQUS, however, is a commercial finite element program that has both thermal and structural capabilities for quasi-static and dynamic problems. The same mesh used for thermal problems can be used for the structural problem. A temperature file is written during the thermal phase of the problem which can be directly read by the structural model. Cracking can be simulated by first bonding all element surfaces together and then letting them "debond" or "crack" if normal stresses exceed a specified level. After debonding, the new free surfaces can slide relative to one another. The criterion for cracking is discussed in a separate section of the report. Though a large number of user subroutines can be written and linked into the code (e.g., non-uniform heat transfer coefficients), the principal disadvantage of using ABAQUS is the lack of access to the source code.

At the outset of this study, the use of the J-integral technique was investigated as part of a process to develop cracks in the structure. For linear elastic materials, the J-integral can be directly related to stress intensity factors. J-integrals can be calculated in the structure and related to critical values which can then be used to open a crack (debond elements). J-integrals can be calculated in ABAQUS. They can also be calculated, using a technique developed by Wellman[23] for the JAC series of codes. The main problem with this technique is that sites where the J-integral is to be calculated must be identified during mesh generation. By itself, this is not a concern. However, in order to calculate the J-integral, a very dense mesh is required around every node. In addition, once cracking occurs, unless a new contact surface is generated at each new surface, the crack surfaces could pass through each other. Doing this would not be possible within ABAQUS and would be a significant development effort within JAC.

As seen from the above discussion, none of the numerical tools will satisfy all the requirements. If there were a clear advantage to any code, the choice of a Sandia-written code would be beneficial. Using a Sandia tool would give the added advantage of changing the source code if warranted. Since cryocycling is a coupled thermoelastic problem, ease of transfer of results from the thermal run to the structural run is important. ABAQUS was the easiest environment to perform this procedure. In addition, ABAQUS offered the opportunity to debond surfaces easily under given criteria. Even though advances were made in the ease of transfer of thermal results in the Sandia codes over the duration of the cryocycling project, it was felt that ABAQUS was the cost effective choice. The implicit time integrator version of the code (ABAQUS-STANDARD) was used to solve the cryogenic problem in a quasi-static manner.

Temperature Environment and Material Properties

--Liquid Nitrogen Heat Transfer Coefficient

Violent boiling occurs when solid propellant at ambient temperature is first immersed in liquid nitrogen. This well known phenomenon occurs because the surface temperature of the propellant exceeds the saturation temperature of the nitrogen. The boiling action actually progresses through three different stages as the propellant's surface temperature approaches that of the liquid nitrogen. Figure 12, adapted from [5], depicts pool boiling behavior for nitrogen. Initially, when the difference in temperature between the propellant surface and the liquid nitrogen is large, film boiling occurs. As the propellant temperature decreases, the heat flux (q/A) also decreases until the transition region is reached. In the transition region, the heat flux experiences a severe increase until the nucleate boiling stage is reached, where the heat flux once again decreases as the temperature of the propellant approaches that of the liquid nitrogen.

Larsen[24] has developed an empirical relationship for the change in heat flux as a function of temperature during the boiling process. This heat flux relation was subsequently used to develop a boiling heat transfer coefficient (h) for liquid nitrogen (Figure 13). The analyses start at room temperature (25°C), corresponding to a temperature difference of 221°C with the liquid nitrogen (-196°C). Surfaces in contact with the liquid nitrogen thus start out near the right end of the curve in Figure 13. As the propellant temperature approaches that of the liquid nitrogen, one moves to the left on the above mentioned curve. At a temperature difference of approximately 30°C the coefficient increases by about 2 orders of magnitude over a relatively small temperature change. This behavior is followed by a change in slope. Such severe non-linearities and rapid variations cause convergence difficulties in the finite element code. These difficulties were resolved by breaking the run into three periods, each of which was prescribed with different time step parameters. Such an approach allows the specification of finer time steps during regions of convergence difficulty.

The functional form of the heat transfer coefficient was incorporated into the analyses via a user subroutine. Such subroutines are written in FORTRAN and can be linked directly into the ABAQUS code. A copy of the subroutine is presented in Figure 14.

Propellant and Explosive Material Properties

In this study we evaluated the effectiveness of cryocycling for three different munitions containing three different propellants/explosives: the ZUNI, Stinger and Falcon. Even though the energetic materials were different, the material properties required to complete an analysis of each system were similar. Material density, conductivity and specific heat were required for thermal analyses. For each of the three systems, we found that temperature-independent values
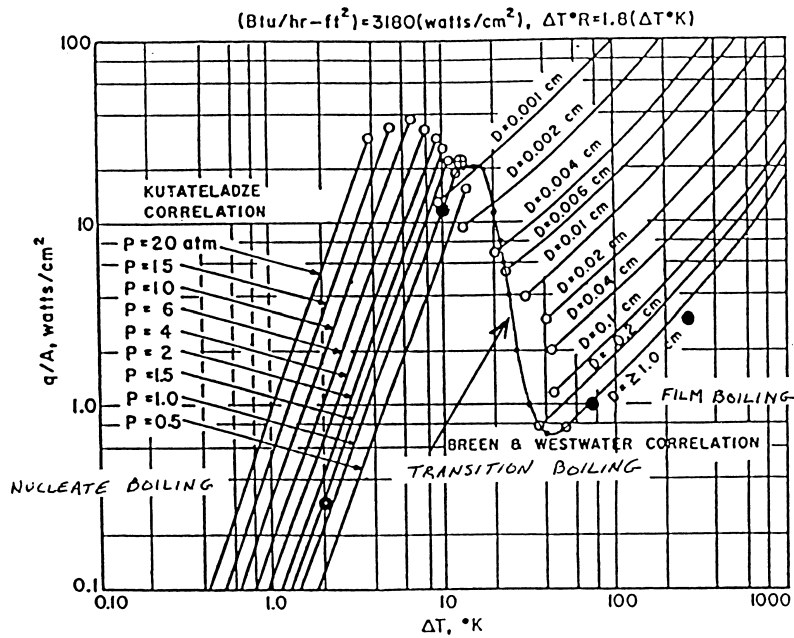
Figure 12. Predictive nucleate and film pool boiling correlations for nitrogen. Adapted from Ref. 5.
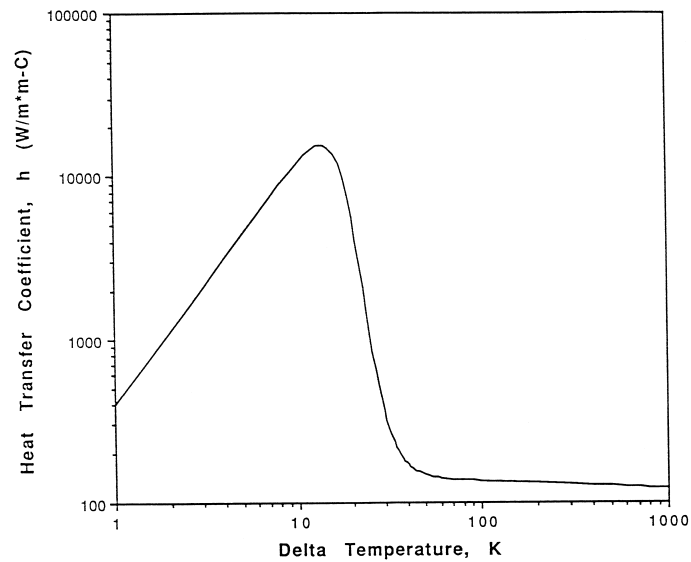
Figure 13. Liquid nitrogen boiling heat transfer coefficient.

36

```
*USER SUBROUTINE
    SUBROUTINE FILM (H,SINK,TEMP,KSTEP,KINC,TIME,NOEL,NPT,COORDS,
    1JLTYP)
    INCLUDE 'ABA_PARAM.INC'
    DIMENSION H(2),TIME(2),COORDS(3)
C
    A=9.628E-9
    B=1.210E-7
    C=5.914
    D=2.494
    F=12.88
    G=1.007E-8
    TBATH=-196.
    DT=TEMP-TBATH+0.
    X=ALOG(DT)
    R=A*X+B
    S=EXP(C*X)
      Y=(R*S+D*X+F)/(G*S+1)
C
    H(1)=EXP(Y)/(DT*1000.)
        H(2)=H(1)*((R*S*C-Y*G*S*C+S*A+D)/(G*S+1)-1.)/DT
    SINK=TBATH
    RETURN
    END
```

Figure 14. ABAQUS Heat transfer coefficient user subroutine.

provided acceptable representations. In the completion of structural analyses, definition of the stress-strain behavior, Poisson's ratio and coefficient of thermal expansion were required. For each system the stress-strain behavior was represented by temperature-dependent properties whereas Poisson's ratio was represented as temperature-independent. The coefficient of thermal expansion was modeled as temperature-dependent in the case of the ZUNI and Falcon, and temperature-independent for the Stinger, based on availability of material data for the wide range of temperatures encountered in cryocycling.

Many of the thermomechanical properties for the energetic materials investigated were not readily available, especially at cryogenic temperatures. For this reason, considerable effort was expended in compiling available information and making educated estimates of material property values. Since each system utilized a different type of energetic material and geometry, they were investigated on an individual basis. A discussion of the material property determination for each system follows.

ZUNI (Extruded X-8 Propellant)
Due to the lack of documented temperature-dependent properties for this propellant (X-8), a material data set was developed based upon a combination the limited X-8 data available[25-27] and that of similar types of propellant. These similar propellants included JPN[28], N-5[29-32] and M8[33]. These propellants have formulations similar to X-8, providing justification for using the available databases of temperature-dependent material properties. The stress-strain representation

of this material included both temperature-dependent yield and ultimate strength behavior. A plot of the extracted stress-strain response is shown in Figure 15.
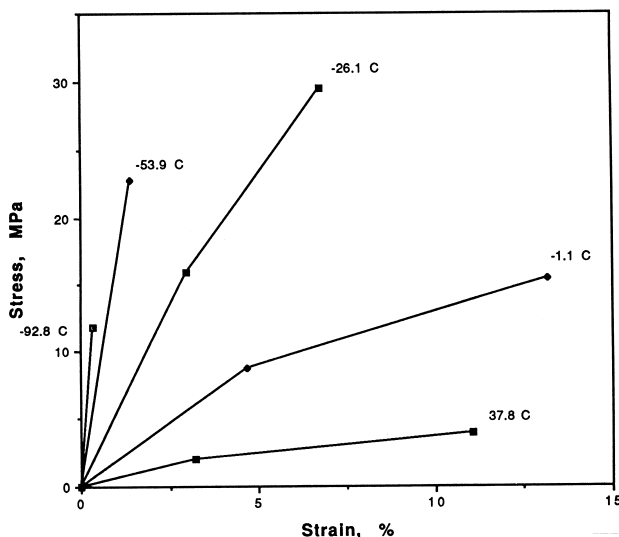
Figure 15. Zuni propellant uniaxial stress vs strain curves used in finite element calculations.

Results from material tests conducted at Thiokol[34] suggest that Poisson's ratio for this propellant is less than 0.5, the value often associated with elastomers. In addition, these tests indicate that the Poisson's ratio may actually vary depending on the strain level, and so may be impacted by failure of the bonds between binder and oxidizer particles. Again, the available data are very sketchy. A value of 0.35 was chosen as a best estimate based upon available data.

A complete listing of the X-8 propellant data used for the ZUNI is contained in Table 1.

Stinger (HTA-3 Explosive)
The Stinger was analyzed following a special request made by the Army Missile Command (MICOM)[35]. A complete discussion of this analysis, including material property determination, is included in the section "Stinger Analysis." In this analysis the stress-strain behavior was modeled as temperature-dependent elastic. A complete listing of the HTA-3 data used for the Stinger weapon is contained in Table 3.

Falcon (TP-L 8237 Propellant)
In establishing material properties for the Falcon propellant data available from TRX-F237[36] was added to the limited data available for TP-L 8237[36]. TRX-F237 is a propellant which has similar constituents as TP-L 8237. A temperature-dependent bi-linear stress-strain relation was established from these data. Poisson's ratio was assumed to be 0.35 based upon tests conducted at Thiokol[37] (see previous ZUNI properties discussion). Since no additional coefficient of

thermal expansion data were available, the values established for X-8 propellant were used. A complete listing of the TP-L 8237 propellant data used for the Falcon weapon is contained in Table 4.

Case-Bonded vs. Propellant-Only Geometries

Most propellant grains analyzed were not bonded to the rocket motor case and were thus easily removed in preparation for cryocycling. For these grains, liquid nitrogen is in direct contact with all external surfaces during the first phase of the cryocycle. However, some propellant grains are bonded to the rocket motor case which can be either metallic or non-metallic, depending on the application. An example is the Falcon rocket motor which has a steel case. Since no easy debonding techniques are available, case and propellant were cryocycled together. For the Falcon, this proved to be a difficult combination for inducing fracture. Several features of the Falcon contributed to this problem: liquid nitrogen was not in direct contact with some of the propellant surfaces, the steel case has a low coefficient of expansion which constrains the propellant, and the composite propellant which has been shown to be resistant to cryocycling.[34]

Cracking Method Using Interface Elements

One method investigated to simulate propellant cracking and case debonding numerically was the use of debonding interface elements. The ABAQUS[17] code allows interface elements to be placed at the adjoining surface between two elements. Debonding of the surfaces then occurs based upon achieving a critical stress (force) at adjoining nodes across the interface as defined by the following relation (for two dimensional elements):

$$f = [(\sigma/\sigma_f)^2 + (\tau/\tau_f)^2]^{1/2}$$

where:

σ = the normal stress component
τ = shear stress component
σ_f = normal failure stress
τ_f = shear failure stress
f = failure function = 1 at failure (within a user specified tolerance)

If elements separate based upon this strength criterion, the element faces can move relative to each other. This movement includes separation, sliding, and subsequent re-contact. The advantages of this technique are that the debonding criteria can be prescribed as a function of temperature and that stress redistribution effects due to crack formation are accounted for. Ultimately, it is desired that a global cracking model would be developed which allows debonding (cracking) between all elements in the propellant and between the propellant and the case.

To investigate the application of this technique in developing a global cracking model, several possible debonding locations were placed within a 'test' finite element model. This test model was developed using the propellant in the ZUNI rocket motor (discussed later), with a fictitious aluminum case bonded to the propellant in order to include all the features in one model. That is, the ZUNI propellant grain model was used, and a fictitious aluminum case 3.0 mm thick was attached with an infinitesimal bond line. The assumed debonding locations were along symmetry

planes, emanating from a free surface, and intersecting within the propellant grain. In addition, the technique was used to model debonding between the propellant and the case. The locations of possible debonding interfaces for this initial study are shown by the heavy black lines in the upper left graphic of Figure 16. The remaining three graphics of Figure 16 depict crack formation as a function of time after the propellant is immersed in the liquid nitrogen. The first cracks that are formed occur at the propellant:liquid nitrogen interface. As time progresses and the thermal gradient proceeds into the propellant, additional surfaces debond (crack) at interior locations. In addition, the propellant and case eventually debond.

Based upon the positive results of this initial investigation, a computer program was written to embed debonding surfaces between all elements of a propellant grain, thereby providing a global tracking model. However, successful completion of a global cracking analysis proved to be problematic. The ABAQUS finite element code was unable to converge on a solution. Extended discussions with ABAQUS support personnel yielded no feasible resolution to these difficulties. Consequently, an alternate method utilizing a user subroutine was developed to track elements exceeding the critical tensile strength

Cracked Element Subroutine

The ABAQUS code allows one to write a subroutine that introduces new output variables defined by the user. A routine to track the number and location of elements exceeding a critical value was incorporated into the analysis utilizing the USER Subroutine option in ABAQUS. This subroutine recorded the time at which any element reached a critical hydrostatic pressure limit, keeping track of the number of elements that had failed at any point in time as well as their location. The pressure at every integration point was monitored to determine if the pressure within an element exceeded a pre-determined tensile strength. When the pressure exceeded the strength, which was a function of temperature, the value of this variable was set to a value associated with failure. In this manner, one could post-process an analysis, producing contour plots of this binary damage variable. A "zero" value would indicate "no failure", while a "one" value would indicate damage. The "zero" value would be plotted in one color while the "one" value would have a different color. Since these elements were not removed from the calculation, it was possible for them to cycle through a decrease and then an increase in pressure. Once the critical hydrostatic pressure is reached in any given element, subsequent cycling to this value are not counted by the routine (avoiding double counting). In this method, the structural analysis does not account for the possible effects of stress redistribution due to crack formation.

Case Bonded Double Base Propellant

127 mm Rocket Motor

Cooling Time -> 0 sec
Displ. Mag. -> 5.0

Cooling Time -> 22 sec
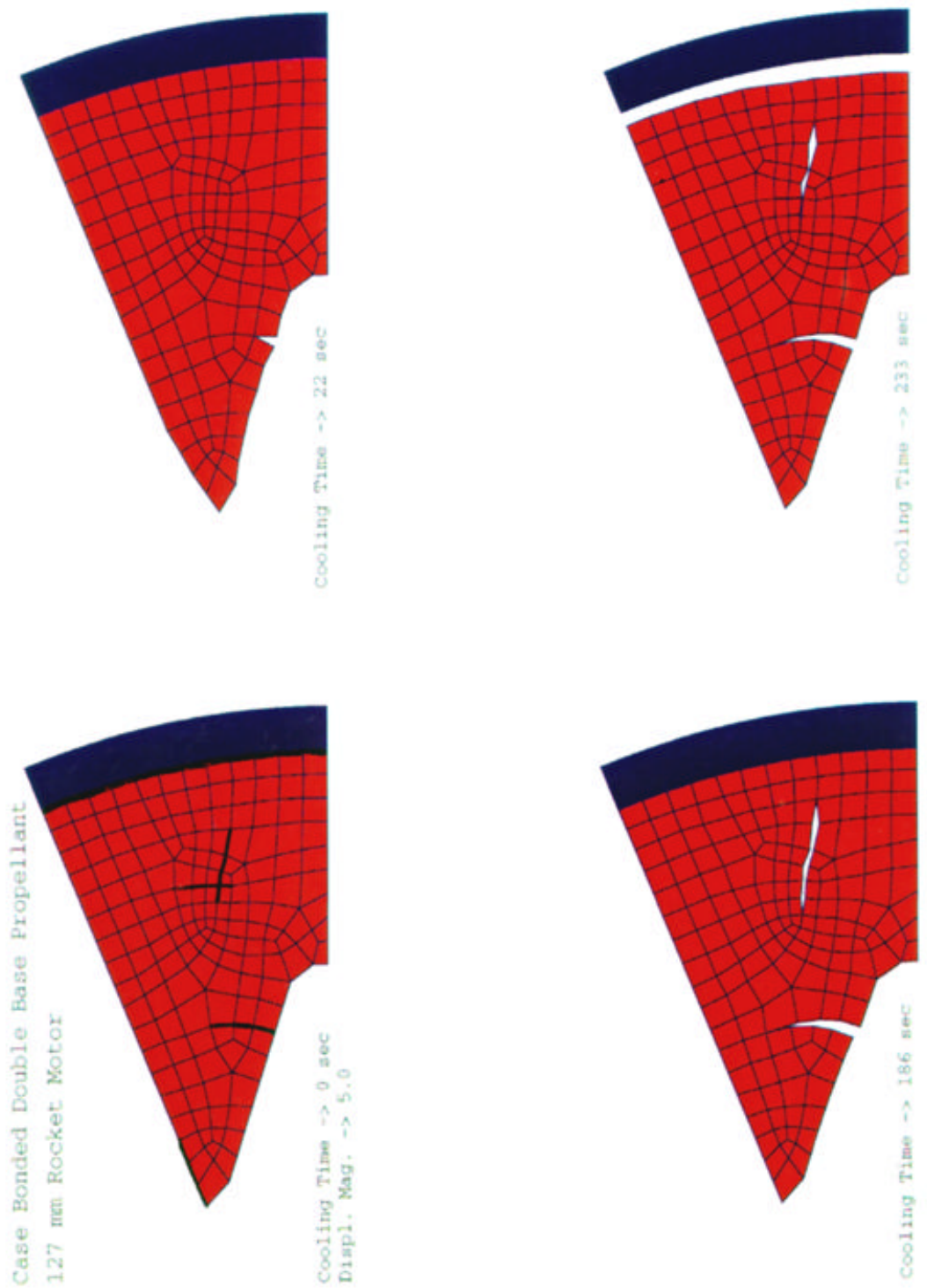
Cooling Time -> 186 sec

Cooling Time -> 233 sec

Figure 16. Cracking and debonding simulations for "case-bonded", double based propellant (ZUNI) grain, using limited number of cracking elements.

Thermo-structural modeling

PATRAN3.0[38] software was used to construct the finite element models of the propellant grains. Two dimensional, plane-strain models were used (i.e., it was assumed that end effects can be neglected). Although cross-sections will invariably not remain plane near the ends of the grain, the primary purpose of this analysis was to provide some understanding of the main parameters affecting the formation of cracks. The detailed stress distributions associated with end effects were therefore not needed. This assumption is also reasonable because the length of a grain greatly exceeds its diameter. Symmetry boundary conditions were used to reduce the model to only a portion of the cross-section (typically 1/16 or 1/8) to minimize computational time.

The analytical predictions of time-dependent thermal and stress fields were computed with the ABAQUS finite element code. Each analysis requires a thermal and a structural analysis, run in series. The thermal analysis provides a thermal history of the entire model which is used as a time dependent loading condition for the calculation of resultant stresses by the structural portion of the analysis. Material properties were developed based on combinations of data that were available for similar propellants, as discussed above.

In the thermal model, the thermal boundary conditions resulting from either contact with liquid nitrogen in the cooling phase, or with ambient air during warm up, are prescribed onto the geometry. The thermal analysis requires material properties of density, conductivity, specific heat, and a boiling heat transfer coefficient.

The structural analysis uses the thermal history as the loading condition to predict stresses. The structural material parameters include a temperature-dependent elastic modulus, ultimate stress, and coefficient of expansion. The initial method developed for simulating this process attempted to account for the redistribution of stress resulting from formation of specific cracks. The method implemented subsequently does not account for such stress relaxation. This method tracks elements that have failed but does not remove them from the calculation or reduce their strength. It was judged that this level of complexity is consistent with the scope of the analysis and limited availability of relevant material data.

ZUNI Rocket Motor Analysis

The ZUNI is one of several rocket motor types in Sandia's inventory. The grain is 125 mm in diameter, 1.3 meters long, with a weight of approximately 13 kg. The cross-section is a right circular cylinder with an internal star configuration. The two dimensional finite element model utilized inherent symmetry in the cross-section shape to limit the modeling to one sixteenth of the grain cross-section. The propellant in the ZUNI rocket motor is X-8. The propellant grain is not case bonded. The X-8 properties used in the analysis (Table 1) were compiled as described in the material property section.

Table 1: Propellant Material: Extruded X-8

Thermal   Analysis Properties

Density	1611 kg/m^3
Conductivity	.208 W/m$^\circ$C
Specific Heat	1444. Joule/kg$^\circ$C

Structural Analysis Properties

Elastic Curve Definition	E (Pa)	Poisson's Ratio	Temp. $^\circ$C
	$3.248*10^9$	.35	-92.8
	$1.622*10^9$	.35	-53.9
	$.536*10^9$	.35	-26.1
	$.186*10^9$	.35	-1.1
	$.0621*10^9$	.35	37.8

Temperature Dependent Plasticity	Yield Stress (Pa)	e_p	Temp. $^\circ$C
	$11.88*10^6$	0.	-92.8
	$22.72*10^6$	0.	-53.9
	$15.96*10^6$	0.	-26.1
	$29.51*10^6$	$1.26 *10^{-2}$	-26.1
	$8.71*10^6$	0.	-1.1
	$15.49*10^6$	$4.86 *10^{-2}$	-1.1
	$1.99*10^6$	0.	37.8
	$3.96*10^6$	$4.68 *10^{-2}$	37.8

Coefficient of Thermal Expansion	Coeff. (e/$^\circ$C)	Temp. $^\circ$C
	$.300*10^4$	-92.8
	$.510*10^4$	-53.9
	$.724*10^4$	-26.1
	$.922*10^4$	-1.1
	$1.150*10^4$	37.8
	$1.315*10^4$	100.0

The analysis found that the majority of the cracking occurs on the outer edges of the propellant where it was in direct contact with the liquid nitrogen. This is consistent with the experimental results which found that three cryocycles were needed to rubblize this propellant to a particle size of 6-10 mm. The vast majority of the cracking also occurred very early in the cooling phase of the first cycle, suggesting that the time of immersion in liquid nitrogen could be shortened. Contours of time-dependent representative variables are shown in Figures 17-19.

Stinger Analysis

During the development of the analytical techniques used in the cryocycling study, a special request was made by the Army Missile Command (MICOM) of Huntsville, AL to analyze cryocycling of the Stinger weapon system[35]. MICOM had been unsuccessful in their attempt to cryocycle the Stinger. The case containing the explosive was immersed in a liquid nitrogen bath for over 30 minutes. However, no failures were observed in the explosive. Sandia was asked to analyze the system with available properties to determine if damage initiation could be predicted.

An axisymmetric model of the Stinger is shown in Figure 20. The geometrical parameters are shown on this figure. There is a titanium (Ti-6Al-4V) case which encloses HTA-3 explosive. The composition of HTA-3 is 49% HMX, 29% TNT and 22% aluminum.[39] The pertinent parameters needed for a thermal and linear elastic analysis are the density, conductivity, specific heat, elastic modulus, coefficient of thermal expansion, and Poisson's ratio. The properties for the Ti-6Al-4V were obtained from Reference 40 are shown below. The only properties which were temperature dependent were the titanium conductivity and the HTA-3 elastic modulus.

Table 2— Material Data for Ti-6Al-4V

$$\text{Density} = 4428 \text{ kg/m}^3$$
$$\text{Conductivity} = 7.8 \text{ J/s} \cdot \text{m} \cdot {}^{o}\text{C at room temperature}$$
$$3.1 \text{ J/s} \cdot \text{m} \cdot {}^{o}\text{C at -196 }{}^{o}\text{C}$$
$$\text{Specific Heat} = 544 \text{ J/kg} \cdot {}^{o}\text{C}$$
$$\text{Elastic Modulus} = 11.4 \times 10^{10} \text{ Pa}$$
$$\text{Coefficient of Thermal Expansion} = .0936 \times 10^{4} \text{m/m/}{}^{o}\text{C}$$
$$\text{Poisson's ratio} = 0.34$$

The properties of the HTA-3 explosive were obtained from References 39, 41, and 42. The elastic modulus at cold temperatures was unavailable in any reference but was assumed to be 3 times the room temperature value for temperatures below the glass transition temperature. This is consistent with other explosives. The conductivity and coefficient of thermal expansion were not
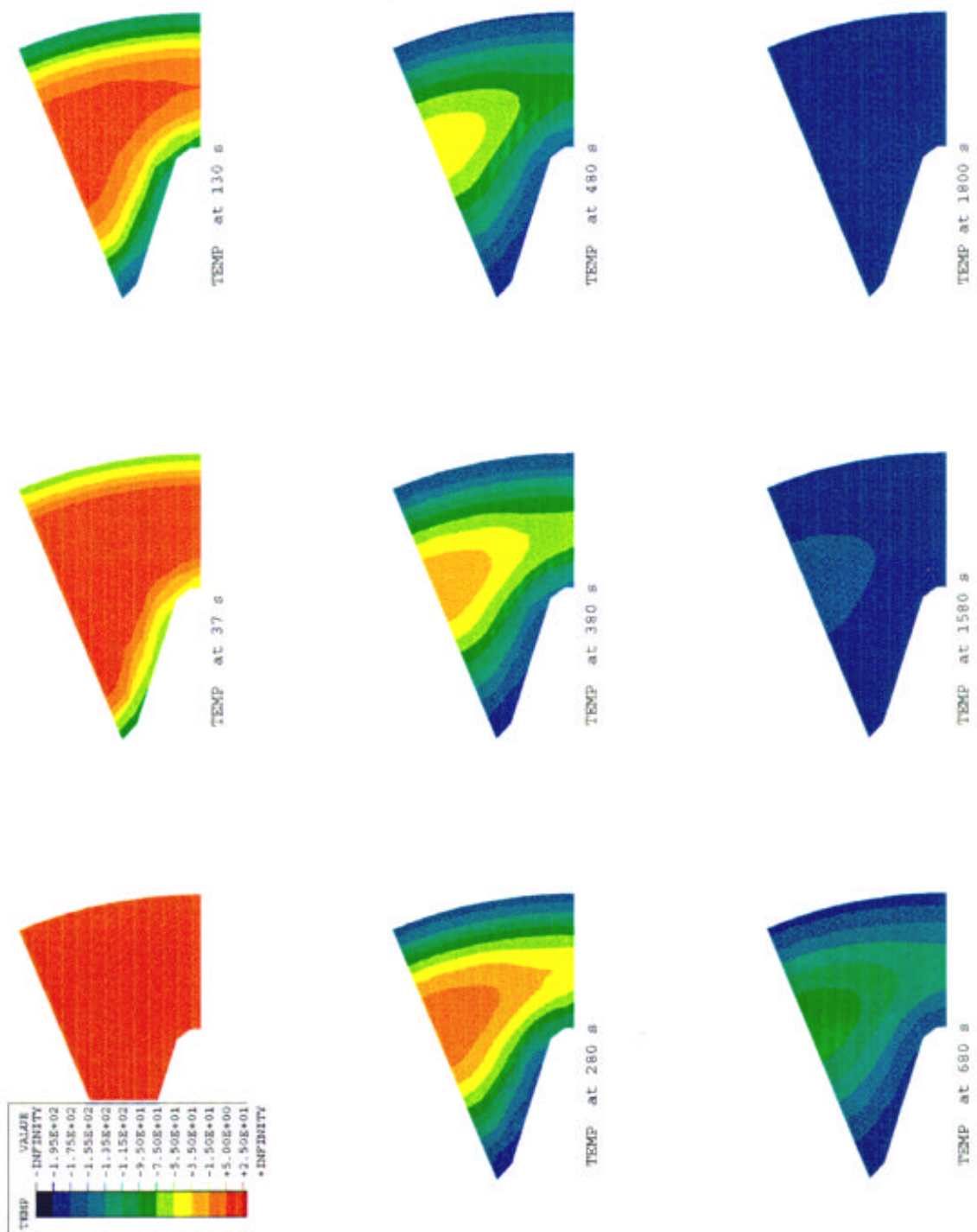
Figure 17. ZUNI grain undergoing cooling in liquid nitrogen bath - temperature profiles.
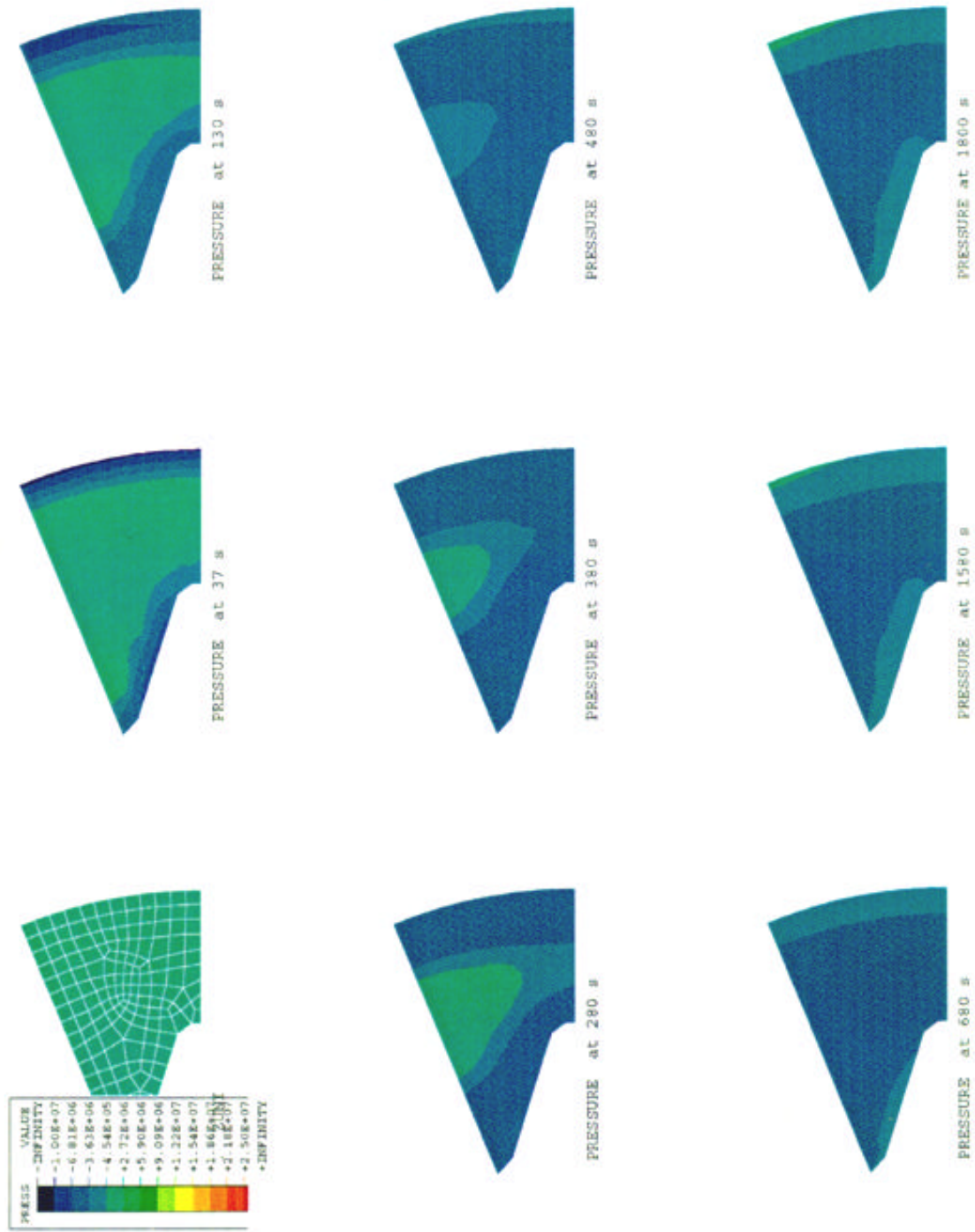
Figure 18. ZUNI grain undergoing cooling in liquid nitrogen bath - resultant pressure.

cracked areas at 0.5 s

cracked areas at 38 s

cracked areas at 180 s

cracked areas at 280 s

cracked areas at 380 s

cracked areas at 480 s

cracked areas at 680 s

cracked areas at 1580 s

cracked areas at 1800 s
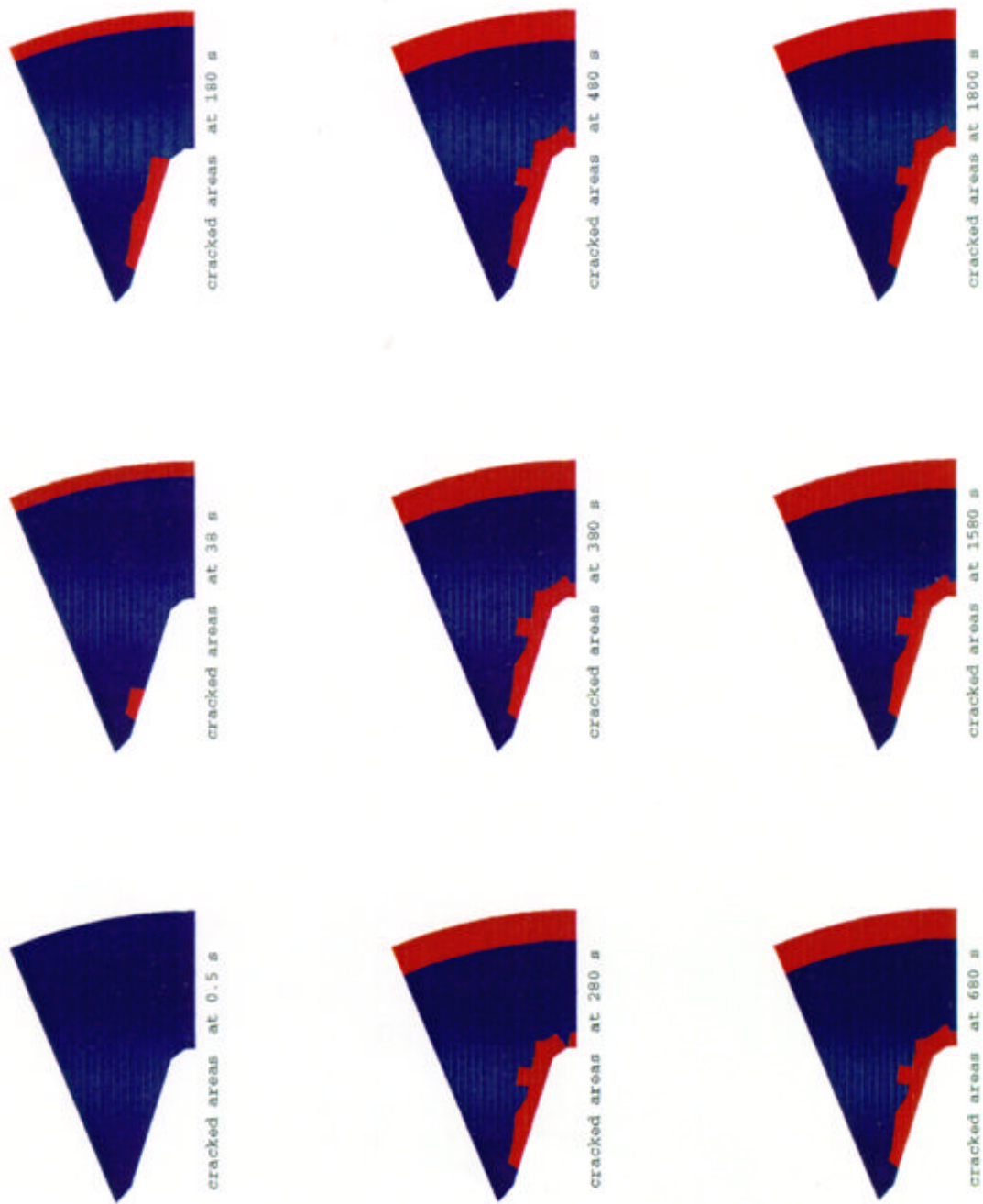
Figure 19. ZUNI grain undergoing cooling in liquid nitrogen bath - cracked areas.

case length=.07757m

case thickness=.00343m

Ti-6Al-4V

HTA-3

case thickness=.00386m

2 =axial

3   1 =radial
3=hoop

r,1=0.

case outer radius = .03485m
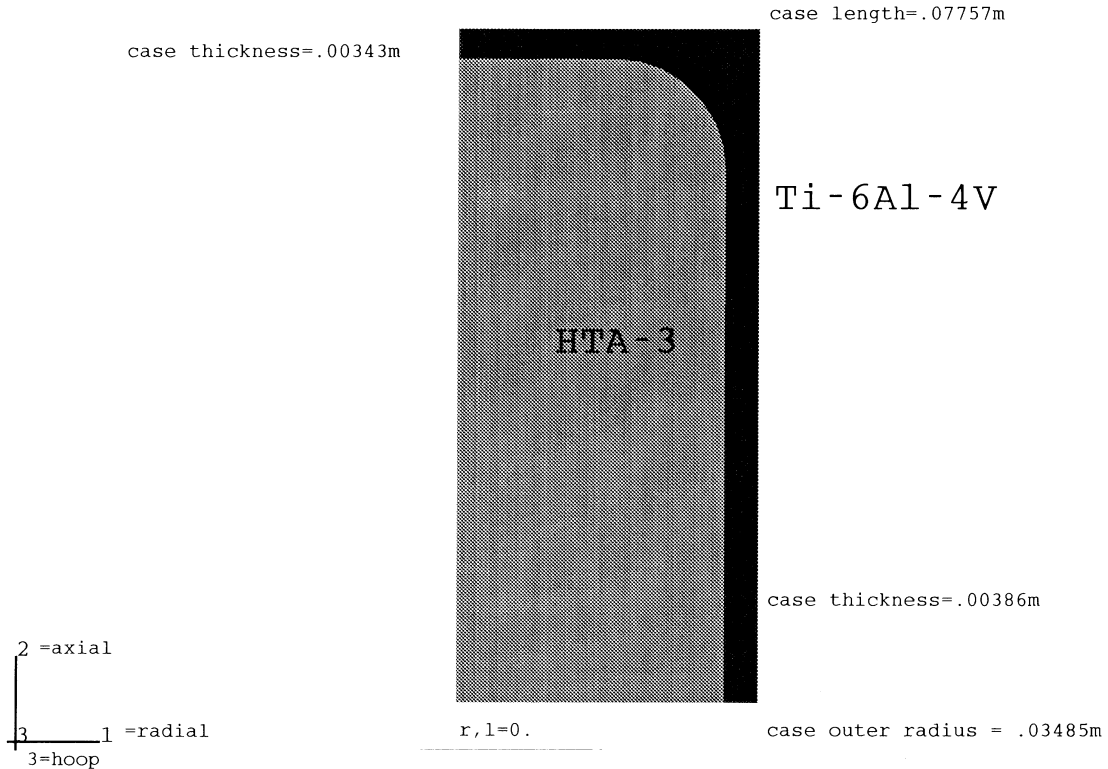
Figure 20. Axisymmetric Model of Stinger case and explosive.

available in any of the above stated references. Therefore estimates had to be made based on known properties ofthe constituents. The properties used for the HTA-3 are tabulated below.

Table 3- Material Data for HTA-3 explosive

Density $= 1900$ kg/ m^3

Conductivity $= 0.4$ J/s•m^{o}C

Specific Heat $=1026$ J/kg^{o}C

Elastic Modulus $= 615$ x 10^6 Pa at room temperature

       1845 x 10^6 Pa at (and below) -100°C

Coefficient of Thermal Expansion $= 5.0$ x 10^5 m/m/^{o}C

Poisson's ratio $=0.45$

Failure Strength $= 1.6$ x 10^7 Pa

The analysis simulated immersion in liquid nitrogen for 30 minutes. The surface boundary conditions were identical to those used for the cryocycling analyses. The results for the temperature distribution are shown in Figure 21 for several times. Note that at 30 minutes, the entire body is close to the liquid nitrogen temperature. Figure 22 shows the predicted values of the stresses (radial, axial, and hoop) and the von Mises stress at 30 minutes in the liquid nitrogen. The proximity of the von Mises stress to the failure stress in brittle materials is often indicative of failure. The only available strength property was the room temperature value for the

Figure 21. Stinger temperature distributions during 30 minutes of cooling in liquid nitrogen.

Figure 22. Stinger stress distributions during 30 minutes of cooling in liquid nitrogen.

compressive strength. The strength was found in Reference 39 and is equal to 2260 psi (approximately 1.6×10^7 Pa). For the purposes of this analysis it is assumed 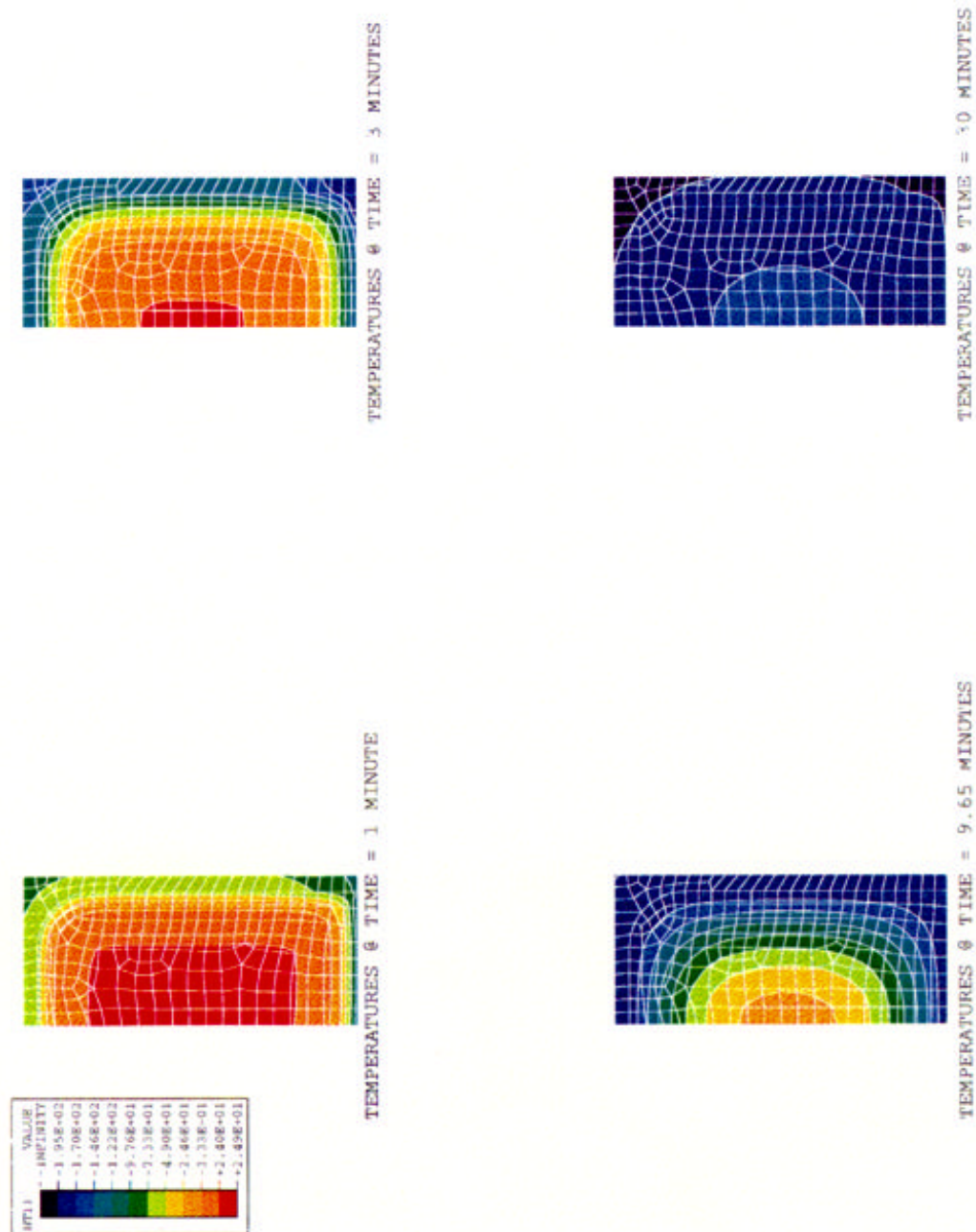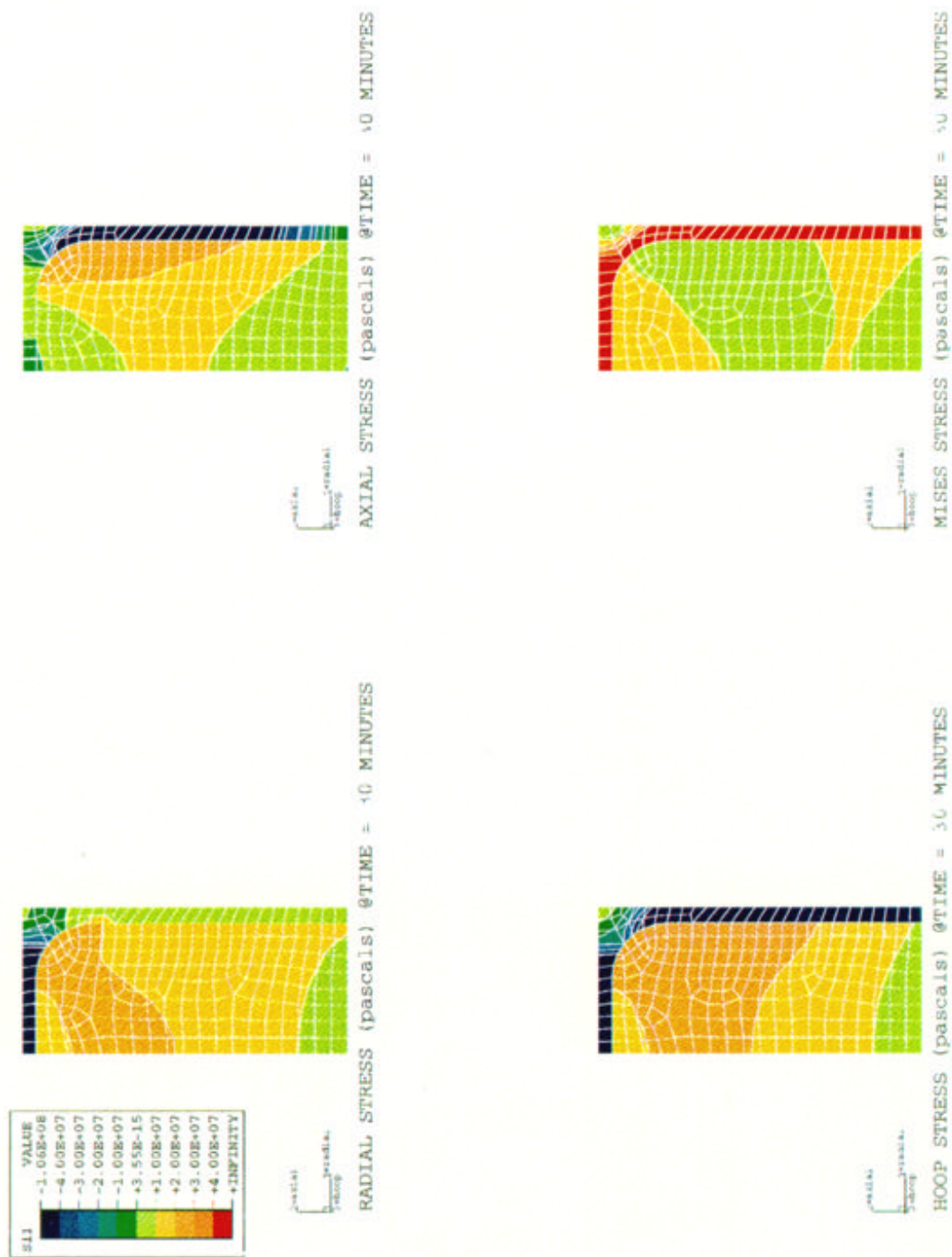that the tensile strength is the same as the compressive strength and is independent of temperature. The surface of the explosive that would be observable after an experiment would be the lower one in Figure 20 (the only explosive surface that does not interface with the titanium. Other than a small part of the surface with high radial stresses, no part of the surface exceeds 1.0×10^7 Pa which is below the strength value assumed. There are some areas internal to the explosive that exceed 2.0×10^7 Pa. Internal cracks may not extend to the surface. Hence, on the basis of this approximate numerical analysis it is not surprising that no damage was observed during the cryocycling of the HTA-3 explosive in the Stinger case

Falcon - Case Bonded Motor

The propellant in the Falcon Guided Missile rocket motor is case bonded and must consequently be processed with its steel case attached. The grain is 0.93 m long and 147 mm diameter with a total weight of 20 kg. In modeling, geometric symmetry of the grain was used to construct a finite element model of 1/10 of the grain cross-section.

The propellant is TP-L 8237, an ammonium perchlorate polysulfide. Material properties for the propellant (Table 4) were compiled as described in the material property section

Figures 23-25 summarize results of the Falcon analyses, showing the pressure, temperature and cracking history of the 1.5 hr cryogenic cooling and 3 hour warm-up phases. When cryocycling of this rocket motor became difficult, the warm-up phase was added to this analysis to provide additional information that might assist in identifying a more effective processing scenario.

The results from the initial analyses, Fig. 19, indicated more cracking than was evident in the experiment. Note, however that most of the cracking occurred away from the case (outer row of elements), paralleling the experimentally noted difficulty of breaking the propellant away from the case. Given that the failure stress for the propellant through the range of temperatures covered in this process was gathered from a number of sources, the confidence in these numbers was suspect. Modifying the failure stress values at the lower temperatures by 50% (increase) produced minimal cracking at the core of the solid section where it would not be visible in the experiment (Figures 26-28).

Further analyses to investigate the cracking behavior were conducted. The most interesting of these are the results for a model without the steel case. Figures 29-31 show the results indicating much less cracking than when the case is present. These cracks also formed toward the end of the warm-up phase. We conclude from the results of the Falcon motor analysis that TP-L 8327 composite propellant is much more difficult to cryocycle than the other propellants and explosives anayzed in this study.

Table 4- Falcon Propellant Material Data: TP-L 8237

Thermal   Analysis Properties

Density	1705 kg/m^3
Conductivity	.32 W/m^{o}C
Specific Heat	628 Joule/kg^{o}C

Structural Analysis Properties

Elastic Curve Definition	E (Pa)	Poisson's Ratio	Temp. ^{o}C
	6.201*10^9	.35	-196.
	6.201*10^9	.35	-150.
	.159*10^9	.35	-68.
	.032*10^9	.35	-50.
	.010*10^9	.35	-18.
	.0062*10^9	.35	+25.

Temperature Dependent Plasticity	Yield Stress (Pa)	Temp. ^{o}C
	24.8*10^6	-196.
	24.8*10^6	-150
	12.3*10^6	-68
	3.5*10^6	-50.
	1.9*10^6	-18
	1.24*10^6	+25.

Coefficient of Expansion	Coeff. (e/^{o}C)	Temp. ^{o}C
	.30*10^{-4}	-92.8
	.51*10^{-4}	-53.9
	.724*10^{-4}	-26.1
	.922*10^{-4}	-1.1
	1.15*10^{-4}	37.8
	1.315*10^{-4}	100.0

Figure 23. Falcon grain undergoing cooling in liquid nitrogen bath and warm-up in ambient air - temperature distributions.
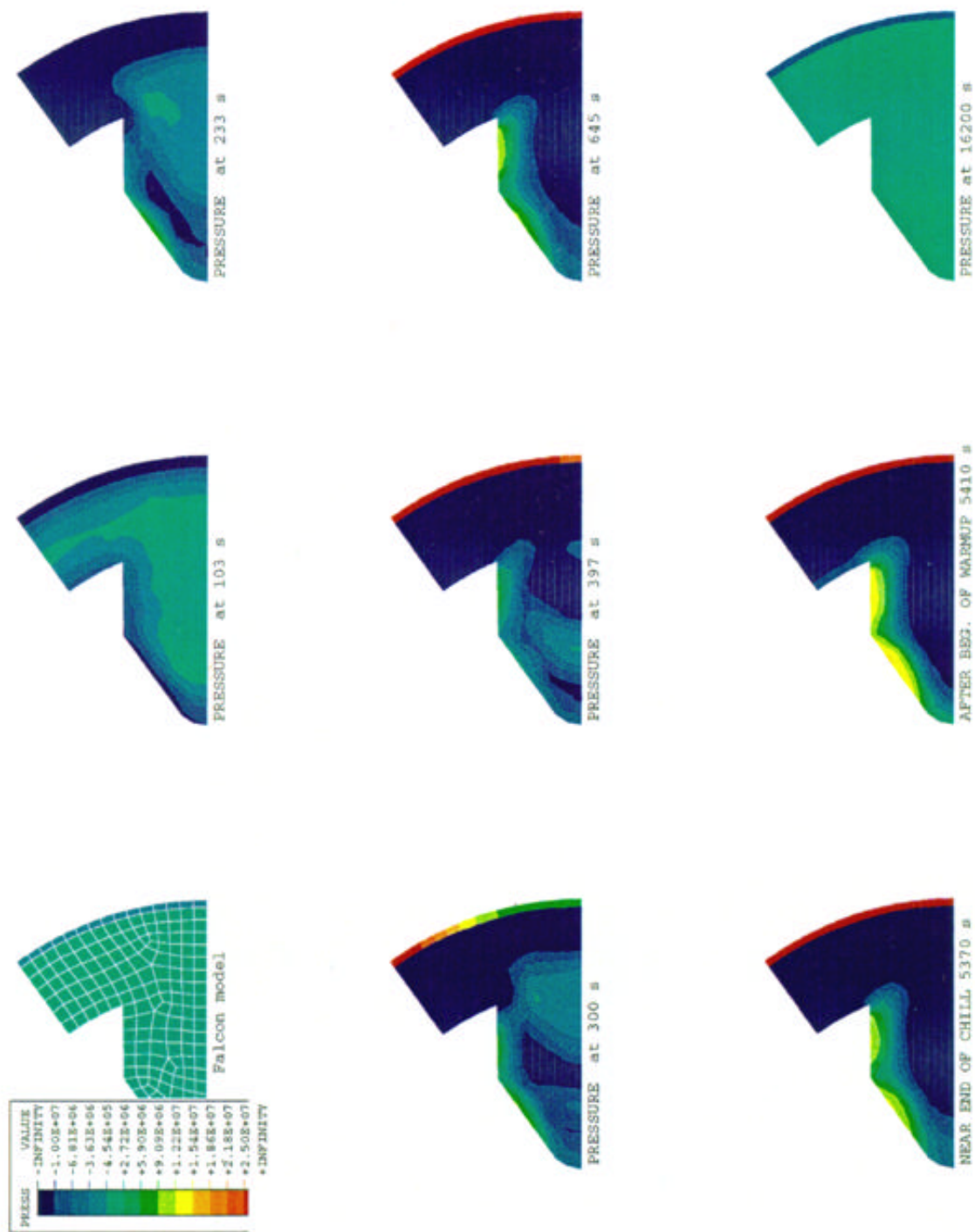
Figure 24. Falcon grain undergoing cooling in liquid nitrogen bath and warm-up in ambient air - pressure distributions.

Cracked Areas at 253 s

Cracked Areas at 103 s

Falcon mod 0

Cracked Areas at 645 s

Cracked Areas at 397 s

Cracked Areas at 300 s

Cracked Areas at16200 s

Cracked Areas atAFTER BEG. OF WARMUP 5410 s

Cracked Areas atNEAR END OF CHILL 5370 s
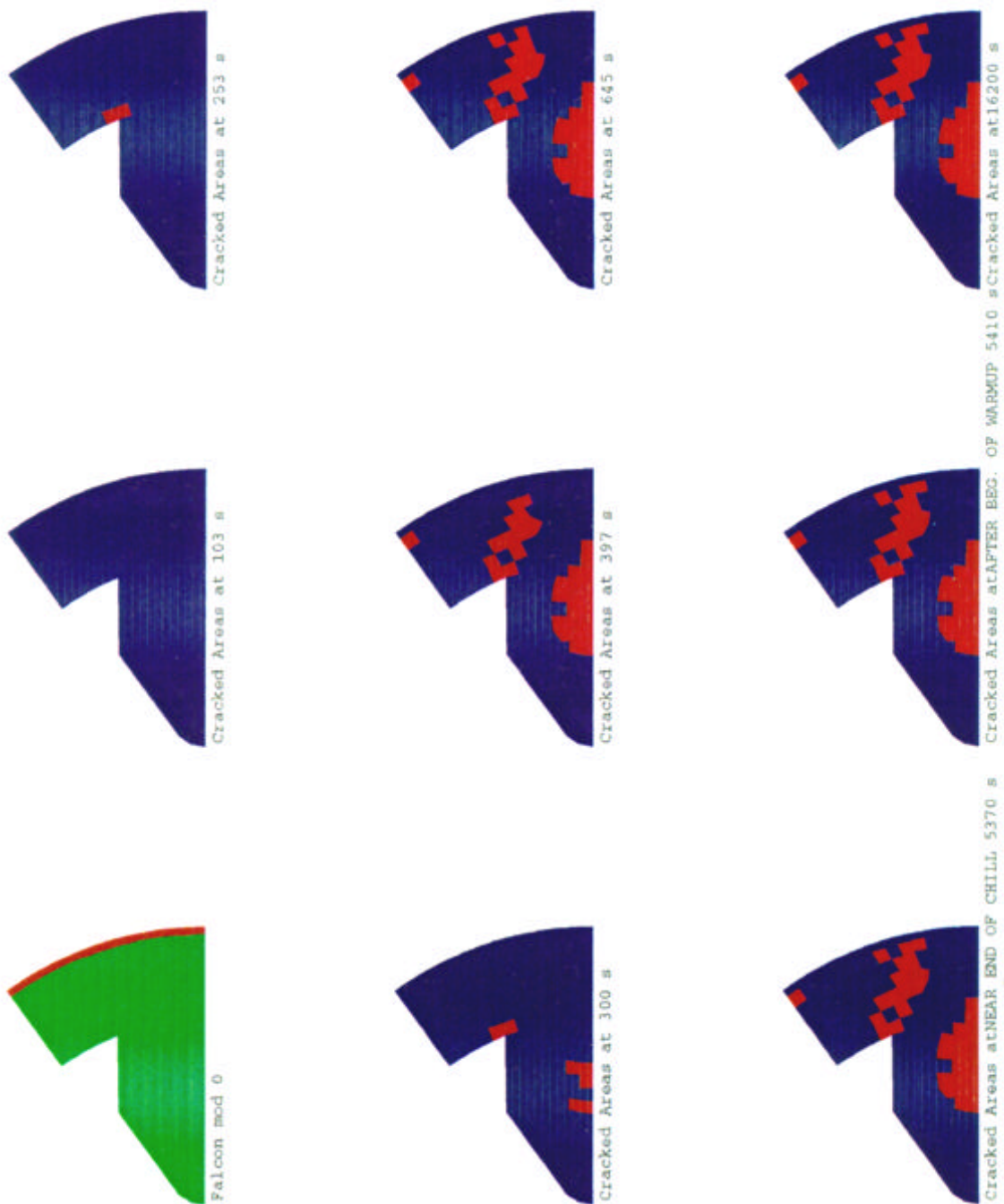
Figure 25. Falcon grain undergoing cooling in liquid nitrogen bath and warm-up in ambient air - cracked areas.

54
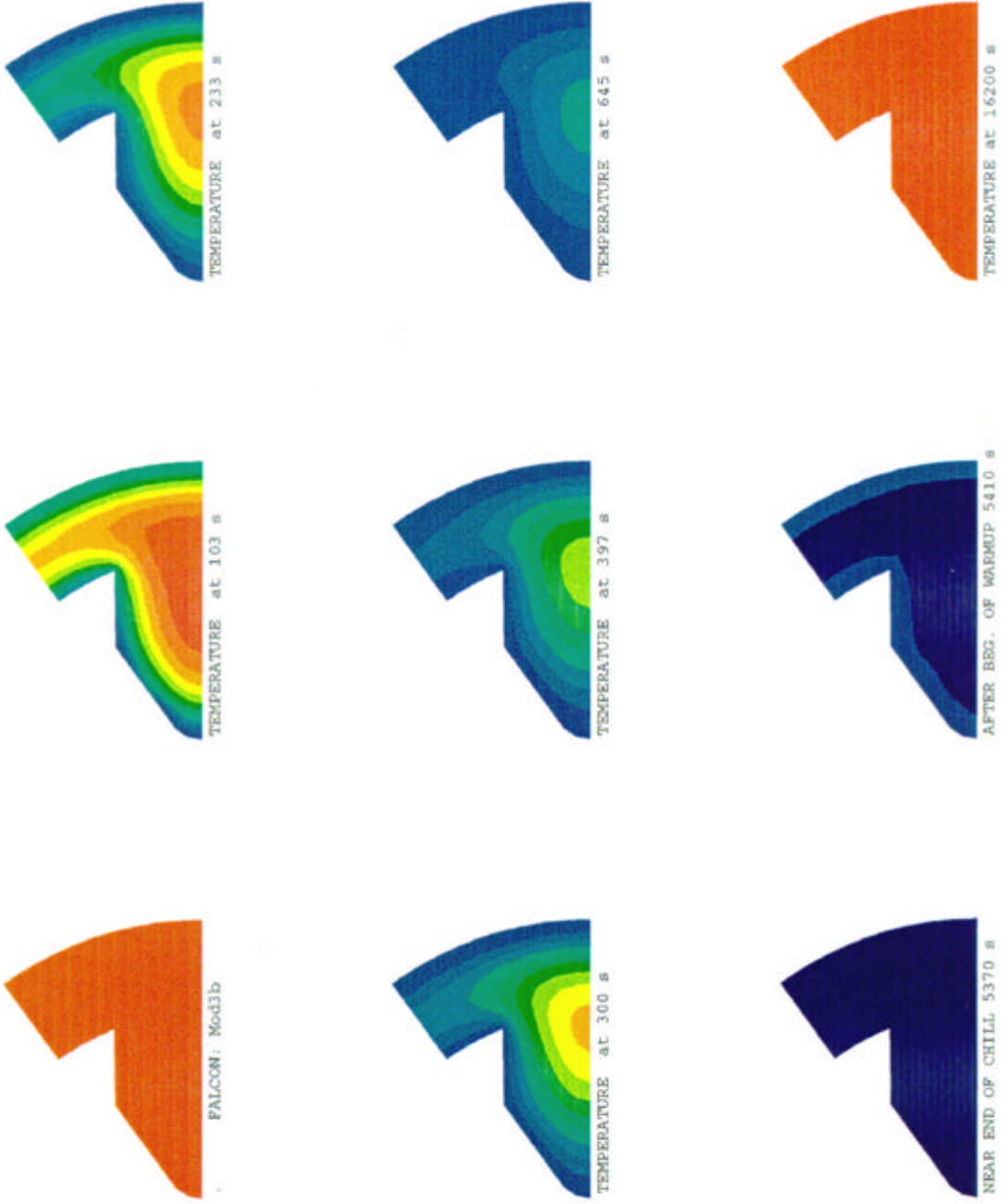
Figure 26. Falcon – using modified failure level - cooling in liquid nitrogen bath and warm-up in ambient air- temperature distributions.
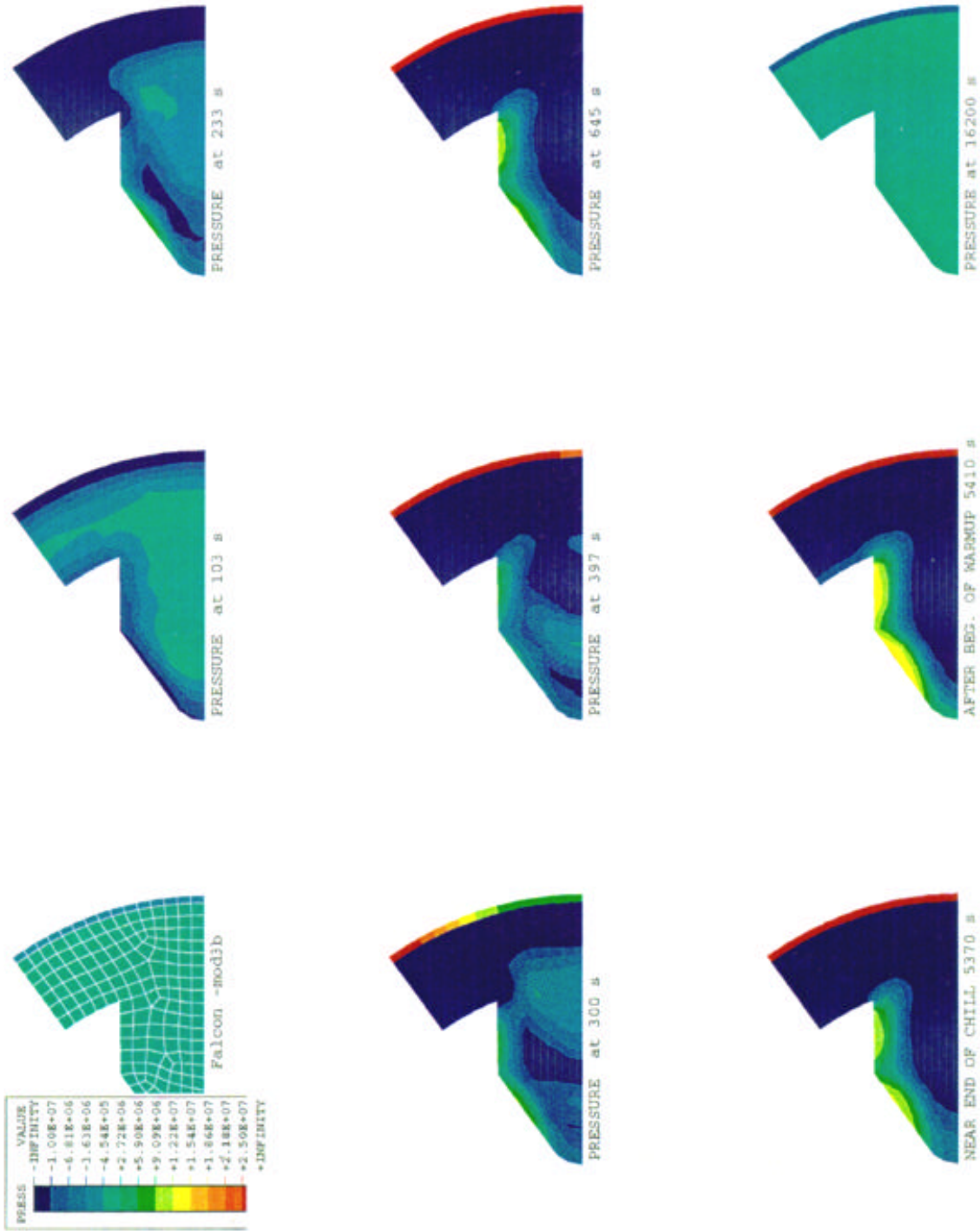
Figure 27. Falcon – using modified failure level - cooling in liquid nitrogen bath and warm-up in ambient air - pressure distributions.
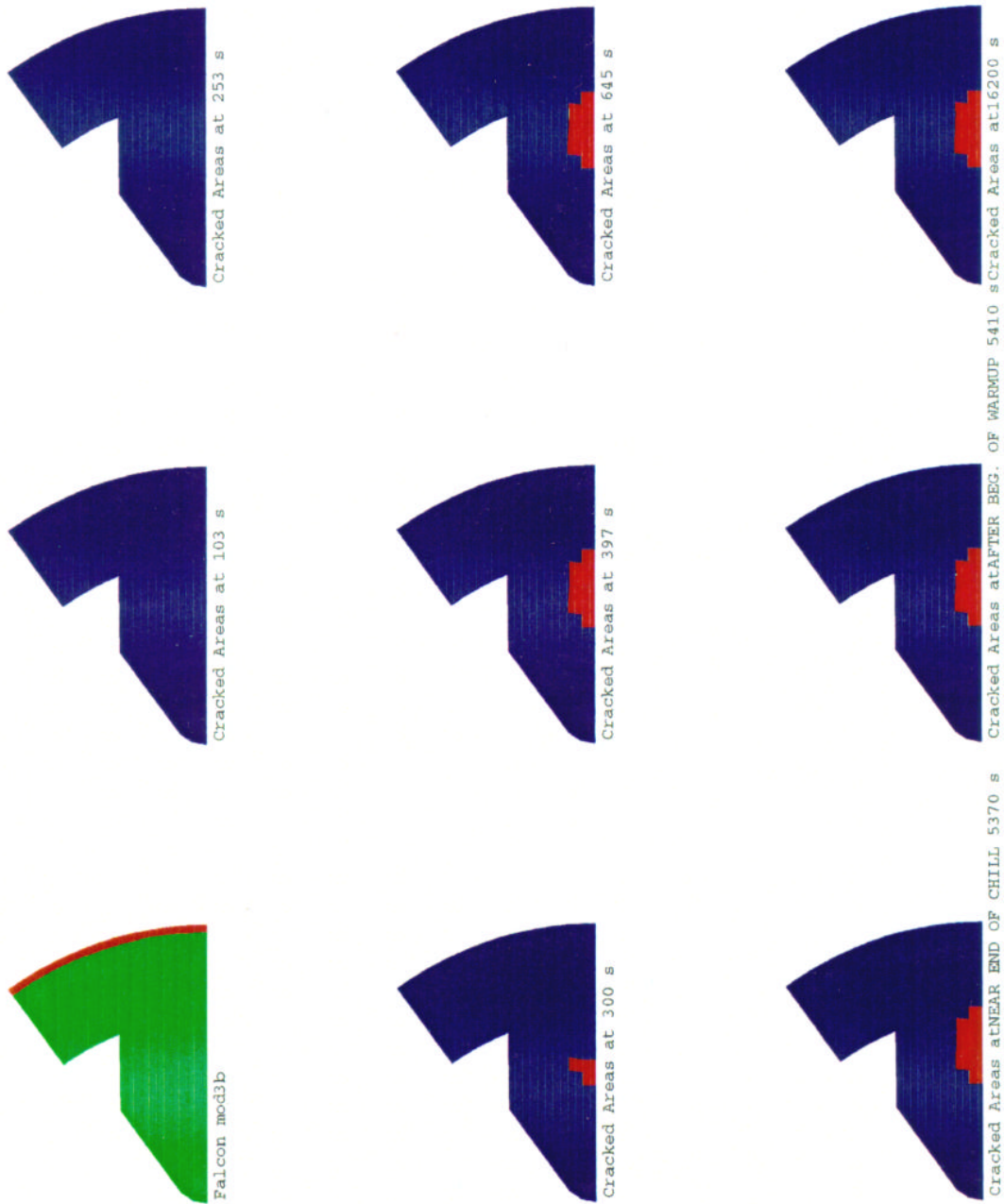
Figure 28. Falcon – using modified failure level - cooling in liquid nitrogen bath and warm-up in ambient air - cracked areas.
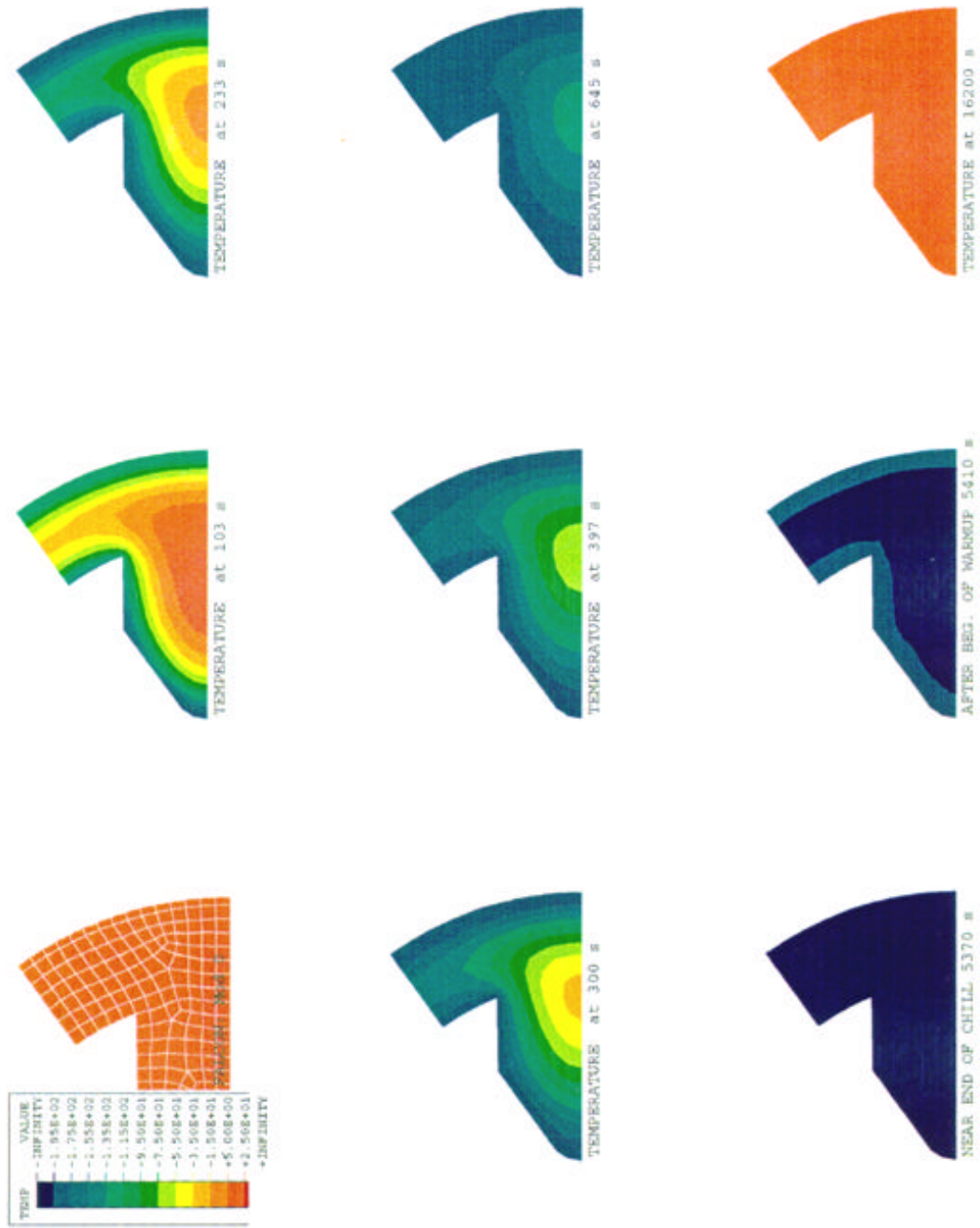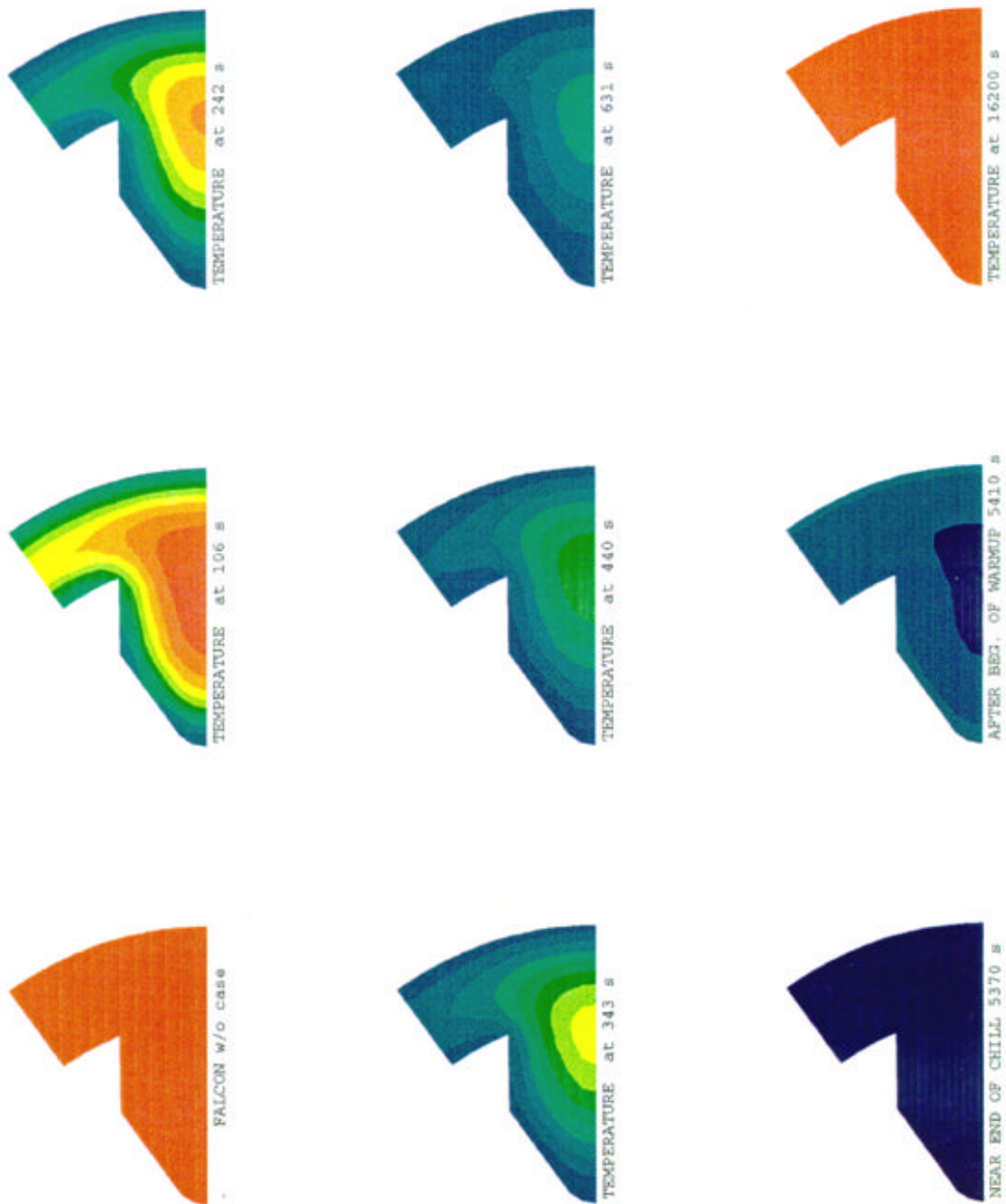
Figure 29. Falcon grain - without case - cooling in liquid nitrogen bath and warm-up in ambient air - temperature distributions.
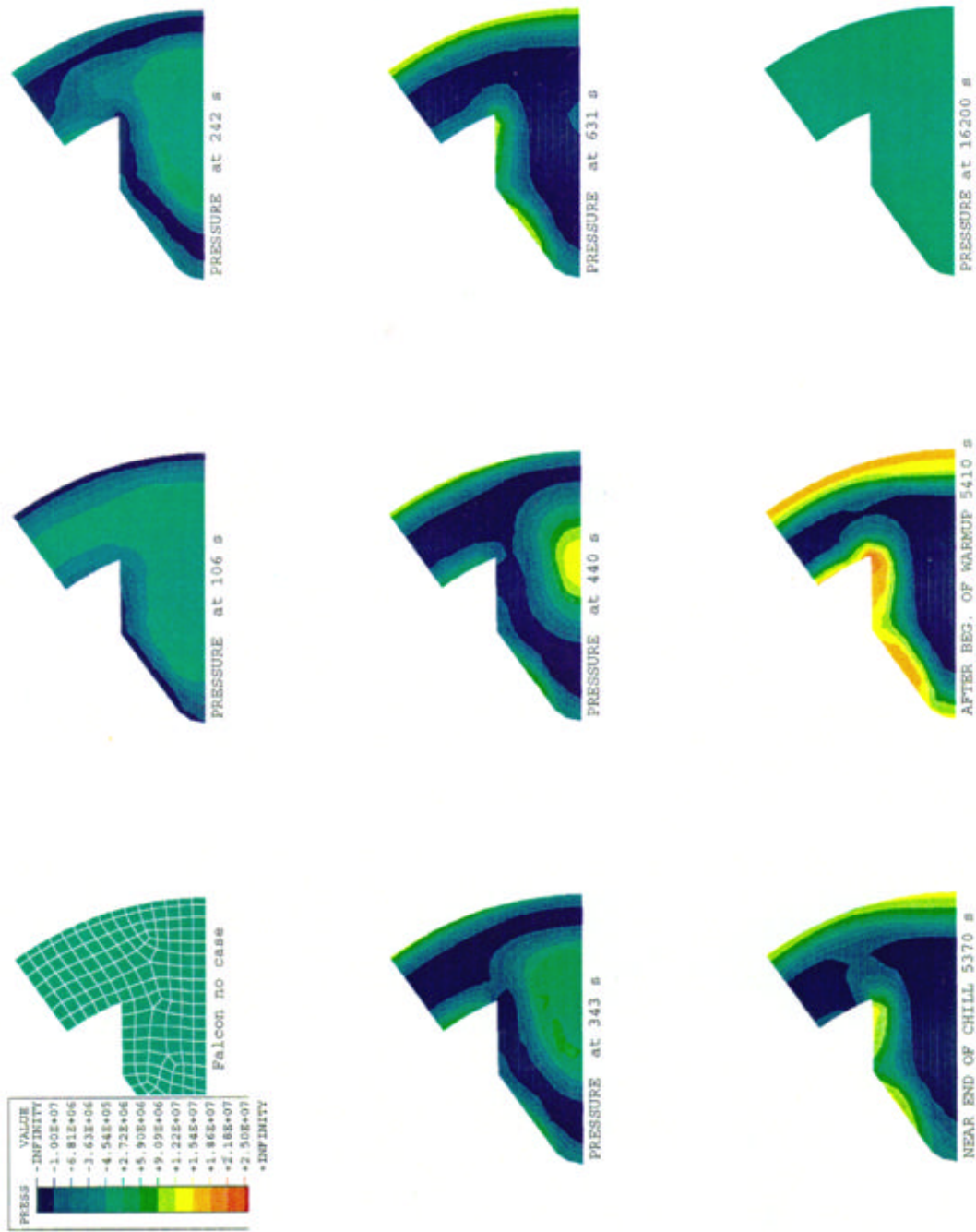
Figure 30. Falcon grain – without case – cooling in liquid nitrogen bath and warm-up in ambient air – pressure distributions.

CRACKED ELEMS at 106 s

CRACKED ELEMS at 242 s

Falcon w/o case

CRACKED ELEMS at 343 s

CRACKED ELEMS at 440 s

CRACKED ELEMS at 631 s

NEAR END OF CHILL 5370 s

AFTER BEG. OF WARMUP 5410 s

CRACKED ELEMS at 16200 s

Figure 31. Falcon grain - without case - cooling in liquid nitrogen bath and warm-up in ambient air - cracked areas.

THERMAL AND MECHANICAL PROPERTIES OF SOLID PROPELLANTS

Realistic numerical models that describe the cryocycling phenomena require knowledge of the thermal and mechanical properties of the solid propellants and inert materials that were used in the tests and evaluations done during the course of this work. In this section, we report the testing techniques and data obtained for the materials of interest

Mechanical Properties

The modulus, ductility, and strength are summarized in Figures 32, 33, and 34 for all inert and live propellants used in our experiments. The data were obtained from several sources. The temperature dependence of the mechanical properties of H-19 and LWCYH was investigated at Sandia National Laboratories. Mechanical properties of polystyrene were obtained from the Encyclopedia of Polymer Science and Engineering. Data for N5 was complied from several sources provided by the Defense Technical Information Center.[43] CYH and JPN data were obtained from the CPIA/M2 Manual.[44] Additional mechanical data for CYH were obtained by Thiokol Corporation under contract with Sandia National Laboratories. All of the data for the QDT, EJC, and VTG propellants were supplied by Hercules, Inc. Mechanical properties for PBX 9404 were acquired from the LLNL Explosives Handbook.[42] The origin of the property data for X-8, TP-L-8237, and HTA-3 is discussed in the section on Analytical Modeling

Thermophysical Properties

Thermophysical properties of LWCYH and H-19 were determined under contact with R.E. Taylor, J.B. Henderson, and H. Groot of the Thermophysical Properties Research Laboratory at Purdue University. Thermal data for CYH were obtained under contract with Thiokol, Inc. Thermal data for N5 and JPN were obtained from the CPIA/M2 Manual. Hercules, Inc. provided the data for the QDT, EJC, and VTG propellants. Lawrence Livermore National Laboratory furnished the thermal data for PBX 9404. The origin of the property data for X-8, TP-L-8237, and HTA-3 is discussed in the analytical section. The coefficient of linear thermal expansion, thermal conductivity, specific heat, and thermal diffusivity are shown in Figures 35-38.

The thermophysical properties of the propellants appear to follow similar trends over the temperatures measured. There are several cases where the range of values for a given property, thermal conductivity for example, are very different for each material, but each generally decreases approximately 40% in the temperature range of -100°C to 50°C.
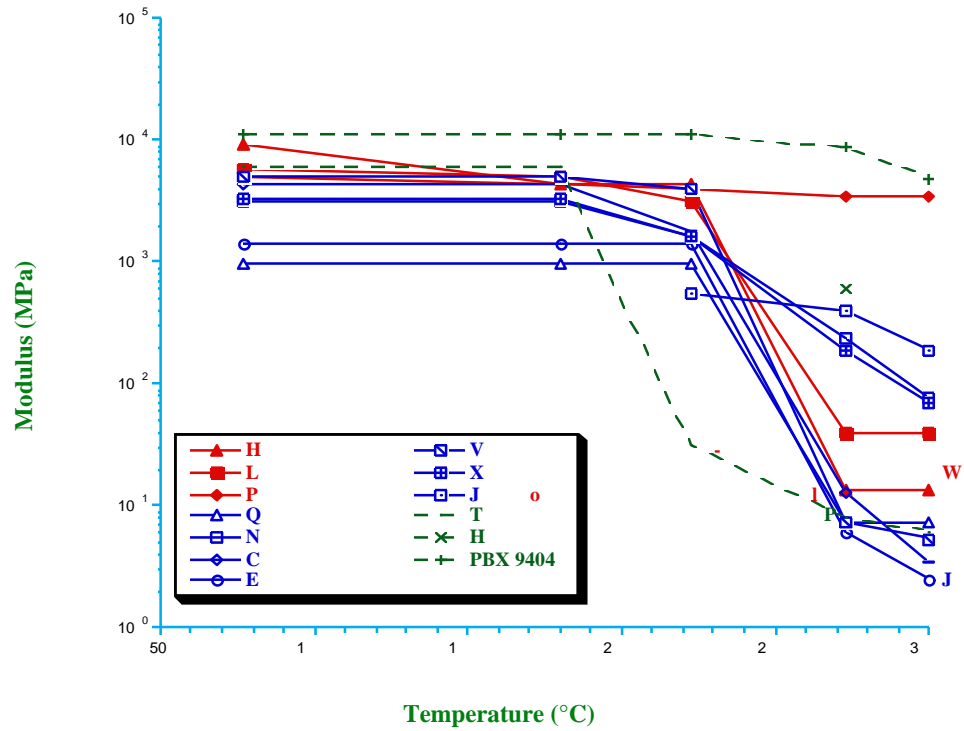
Figure 32. Compilation of modulus data.
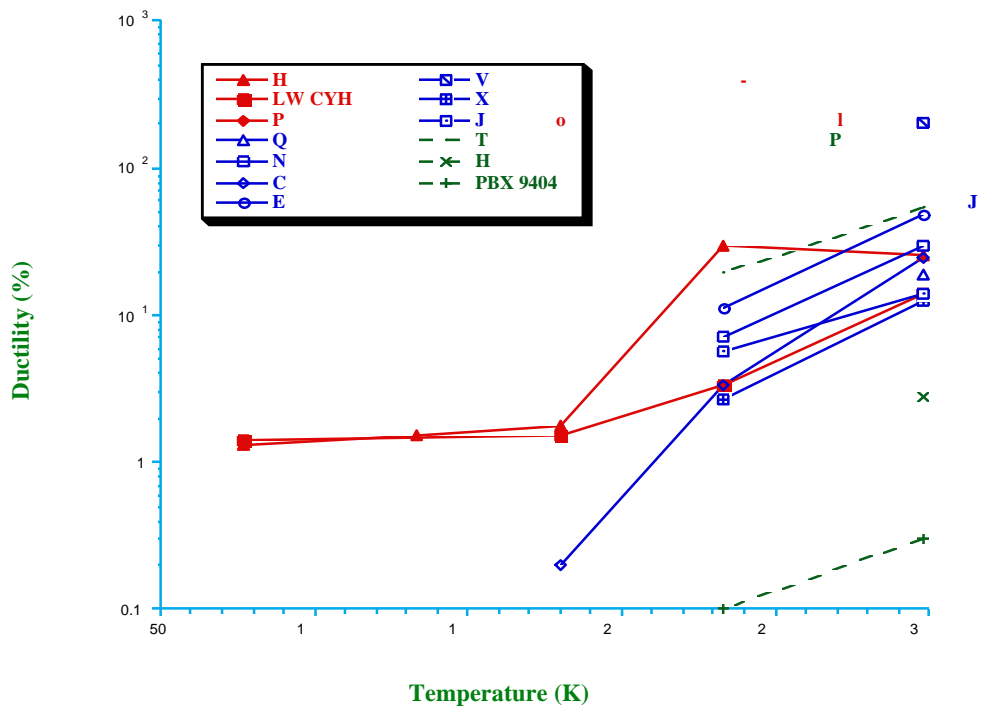
Figure 33. Compilation of ductility data.
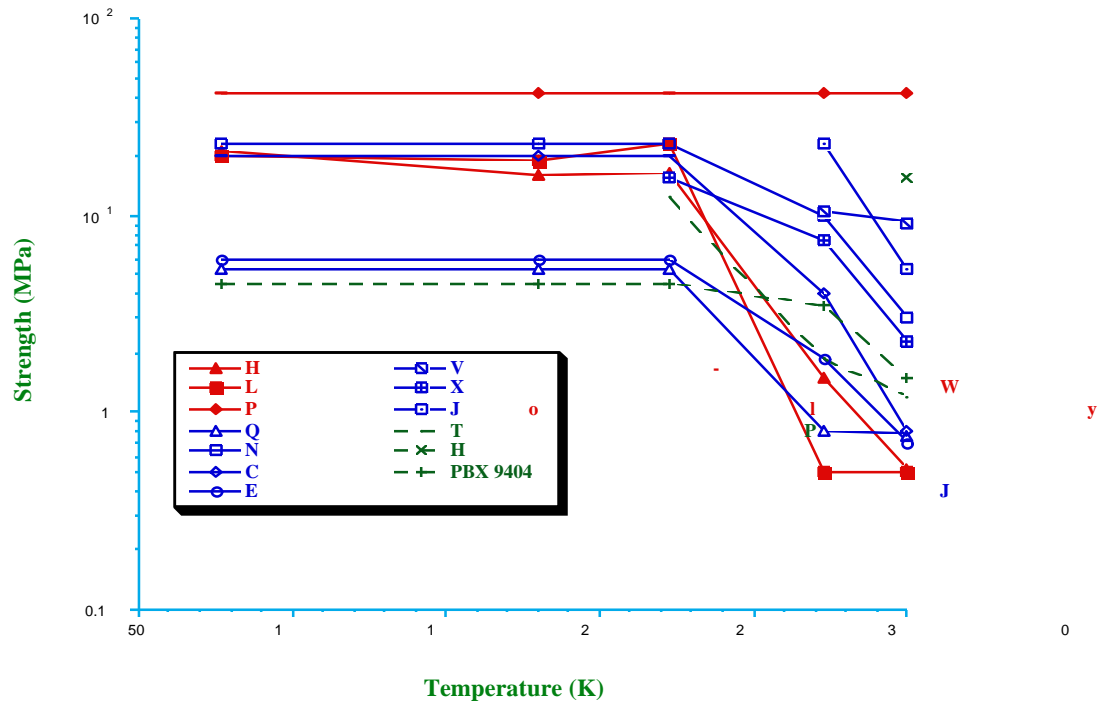
Figure 34. Compilation of strength data.
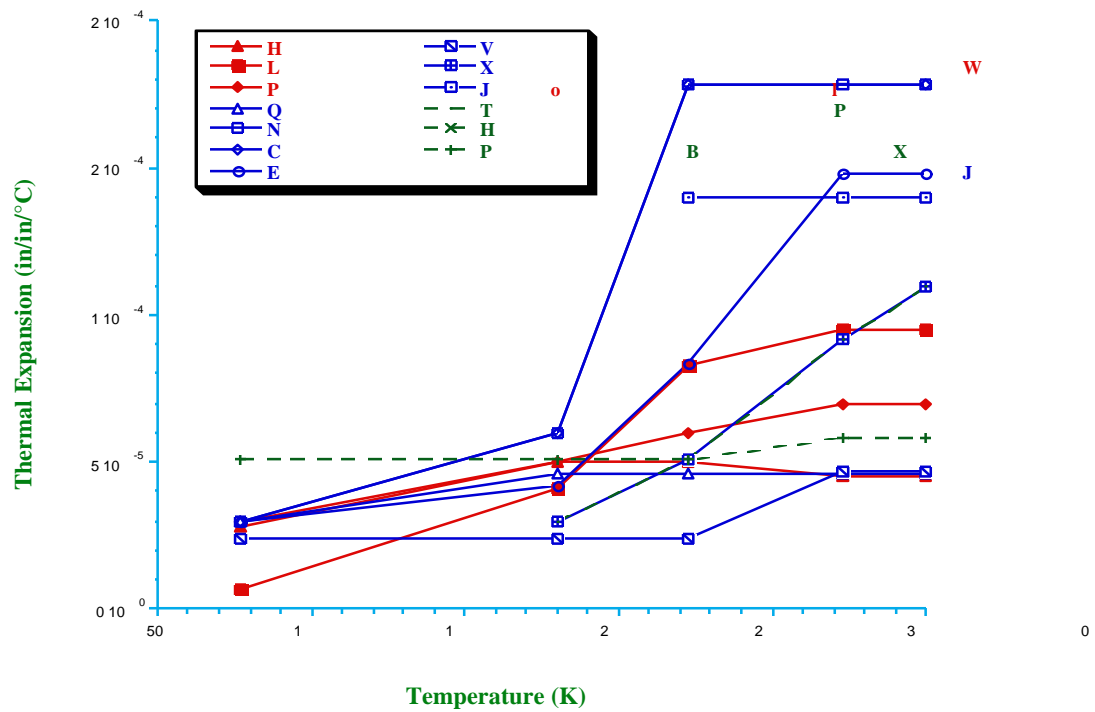
Figure 35. Compilation of linear expansion data.
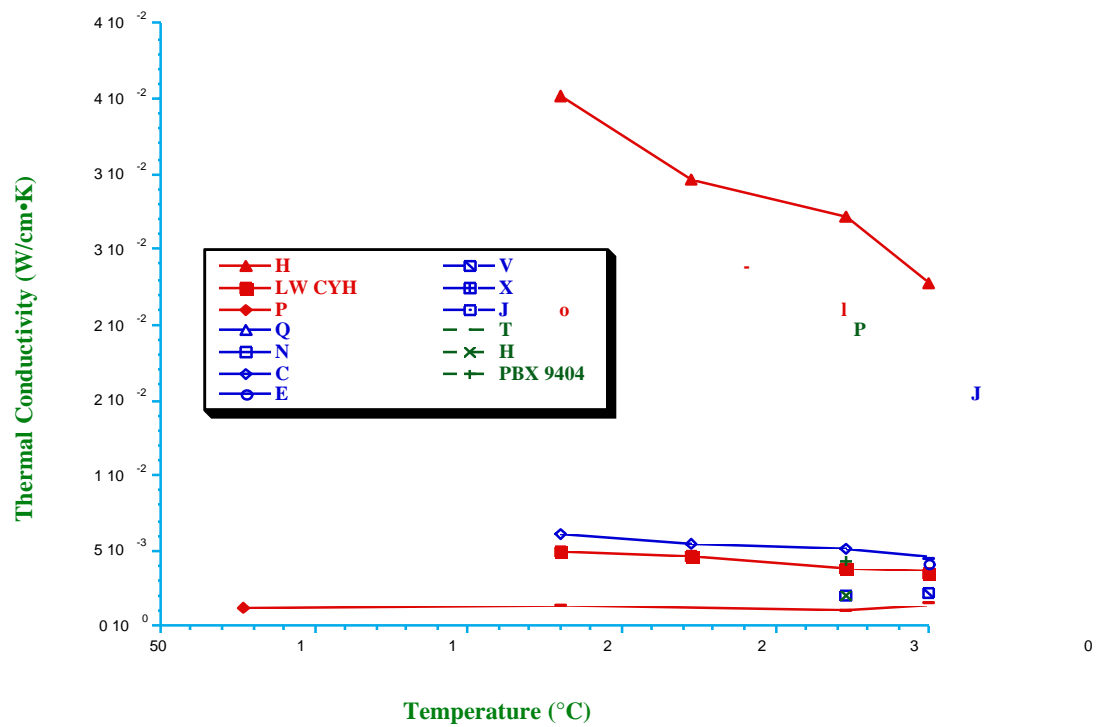
Figure 36. Compilation of thermal conductivity data.
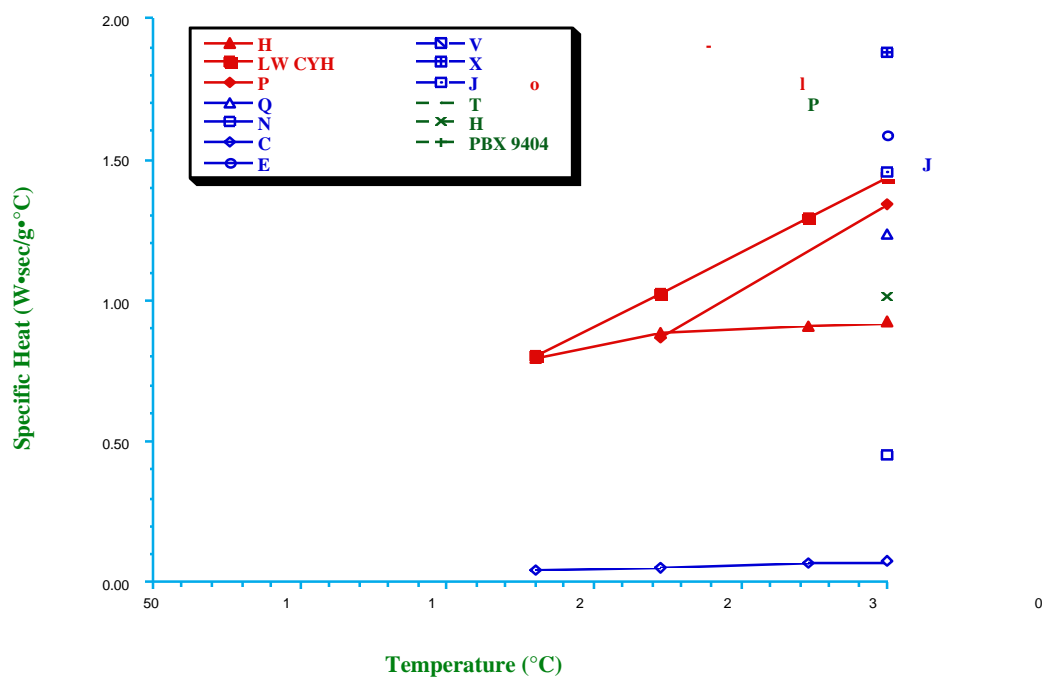
Figure 37. Compilation of specific heat data.
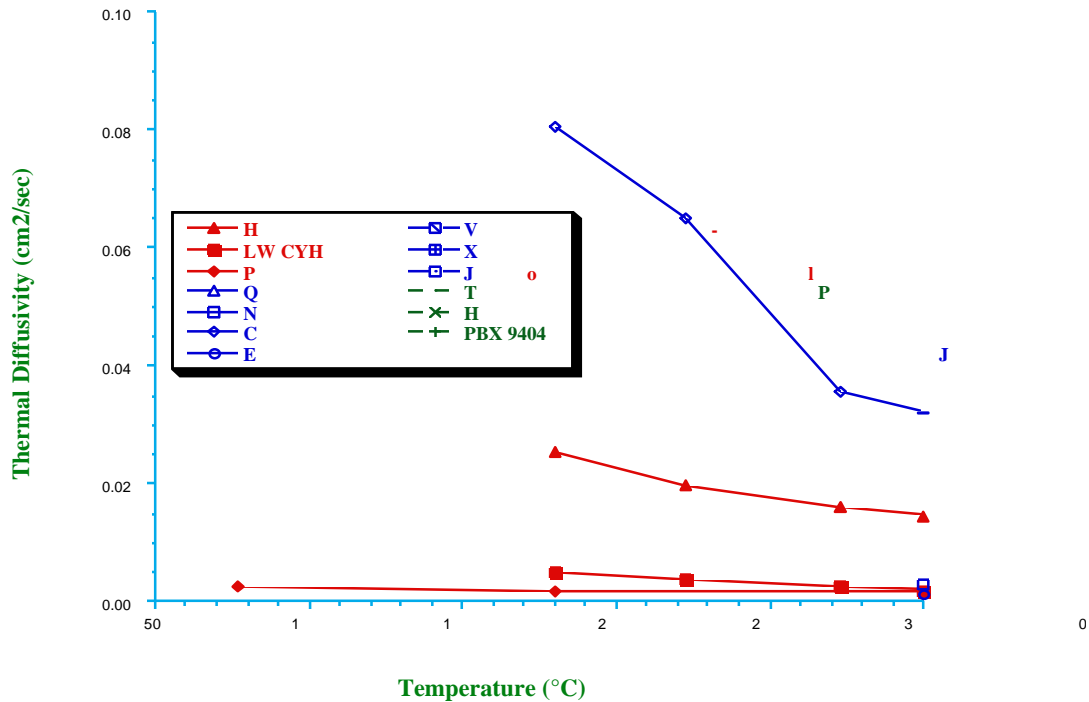
Figure 38. Compilation of diffusivity data.

While it is straightforward to predict the effects of variations in a given physical property, it is much more difficult to predict which set of temperature-dependent physical properties will make a material more or less suitable for cryocycling. For example, we know that a low thermal conductivity will lead to steep thermal gradients. Nevertheless, we have observed that a material with a low conductivity and a low expansion coefficient may not break up as well as a material with a high conductivity and a high expansion coefficient. Since no single physical property exhibits the same temperature dependence for the series of ultimate particle sizes discussed previously, we conclude that no single physical property is dominant in determining the effectiveness of cryocycling. The relative importance of, and the interaction between, all the thermal and mechanical properties of a material with respect to its susceptibility to cryocycling have yet to be fully determined.

ANALYSIS OF DOD DEMILITARIZATION INVENTORY

An analysis of the DoD Resource Recovery and Disposition Account (RRDA) was performed to assess the potential impact of cryocycling on the tactical rocket motor inventory. The analysis aided in selecting candidate tactical rocket motors for demonstrations of cryocycling as an energetic material removal and size reduction process. Munitions placed in the RRDA by the military services are compiled in a handbook known as the Orange Book.[45] The Orange Book is also available in electronic form. Items in the Orange Book are available for resource recovery to other organizations or are identified for demilitarization and disposal. This section summarizes our analysis of the Orange Book.

Requirements for the analysis of data in the Orange Book were:

- identify items fitting the tactical rocket motor category
- identify items representing a significant fraction of the demilitarization inventory in the Orange Book, and
- match cryocycling technology to the identified items

Our analysis began with the March 1994 publication and concluded with the March 1996 publication. The Orange Book lists individual lots of munitions stored in various quantities at military installations around the nation. During our analysis, the number of individual lots ranged from approximately 16,400 to 18,800. Because of the extensive nature of this list, it was necessary to create a special database from an electronic copy of the Orange Book to facilitate the identification of rocket motors that were of special interest to this project. It was also necessary to contact other agencies to acquire information concerning these motors that was otherwise not available in the Orange Book. An example of such information is the chemical composition of the propellant. Information from the Orange Book database and from other sources was compiled in a database that was used to determine the suitability of the listed rocket motors for cryocycling.

The categories of information shown in Table 5 are the basis for the Orange Book analysis.

Table 5. Key Data for Orange Book Analysis

Principal Data	Storage Data	Propellant Data
Motor Type/Model	Location	Designation
Stock Number	Lot Quantity	Type
Length	Total Weight Stored	Composition
Diameter	Condition Code	Method of Manufacture
Weight		Grain Length
Case Material		Grain Diameter
Case Thickness		Grain Weight

The following agencies were instrumental in supplying information for this effort through correspondence and private communication:

- Chemical Propulsion Information Agency (CPIA),
- U. S. Army Defense Ammunition Center (DAC), and
- U. S. Army Armament, Munitions and Chemical Command (AMCCOM)

The CPIA is an information analysis center for the DoD. The center maintains manuals for rocket motors and rocket motor propellants. These manuals provide detailed information on specific items on individual data sheets. The Demil Technology Office of DAC is responsible for the data collection, compilation, and publication of the Orange Book. AMCCOM is the demilitarization

center for the military services and maintains an accounting of the items designated for demilitarization at the various military storage installations.

This effort was performed with the understanding that the quarterly publications of the Orange Book used for the analysis may not accurately reflect current inventory because the RRDA is extremely dynamic. Nevertheless, the analysis provides an understanding of the applicability of the cryocycling technology to the DoD demilitarization inventory. Although many other munition items in the inventory (e.g., projectiles and warheads) contain solid propellants and explosives, this analysis focused on rocket motors because the principal thrust of this project was to develop and demonstrate the cryocycling process for demilitarization of tactical rocket motors.

A summary of information for the five Orange Book publications analyzed from March 1994 to March 1996 is shown in Table 6. The average combined storage weight of all items over this time was approximately 380,000 tons. These items are grouped together as lots containing one munition type. As of March 1996, there were 469 lots of rocket motors stored at various installations with a combined storage weight of 6,800 tons. It should be noted that these weight values represent rocket motor weights in the stored configuration which generally include a storage container and/or other packaging. The 469 lots represent 1.7% of the total weight in the RRDA, which is a significant fraction considering that the percentage would be higher if non-demilitarized motors were subtracted from the inventory, such as those recovered by other organizations or destroyed.

Table 6. Orange Book Data Summary

Orange Book Date	Total RRDA Lots	Total RRDA Storage Weight (Tons)	Rocket Motor Lots > 100,000 lbs.	Rocket Motor Storage Weight (Tons) (Lots > 100,000 lbs.)
3/94	16,382	390,456	23	6,800
9/94	16,383	358,456	16	5,049
3/95	17,334	362,034	19	7,213
9/95	18,719	369,037	22	5,508
3/96	18,831	402,835	21	5,237

Since cryocycling is most efficiently applied in a batch processing mode, it is likely that this demilitarization method will be especially useful at DoD sites where significant numbers of rocket motors are stored. For this reason, our analysis was limited to lot quantities representing 100,000 pounds or more. Applying this criterion to the March 1996 Orange Book, 21 lots of motors, totaling over 93,200 motors, were identified at eight different locations. These 21 lots, with a combined storage weight of approximately 5,200 tons, represent 77% of the total rocket motor weight in the Orange Book. This percentage was 91% and 76% for March 1994 and March 1995, respectively.

A detailed database of the 21 lots was generated to study the suitability of the rocket motors for the cryocycling technology. A summary of the information in the database is shown in Table 7. Ten different types of rocket motors are included in the 21 lots (some of the lots are the same motor type stored at different locations). The motor propellant grains range in diameter from 0.8 to 16.0 inches and range in weight from 1.2 lbs. to 750 lbs. The ten motor types have nine different propellant compositions. Three of the motor types have case-bonded grains and six are cartridge-loaded. The total propellant weight included in the ten motor types is approximately 1,648 tons.

The propellant composition and manufacturing method are of interest because the first application of cryocycling as part of a demilitarization process will be greatly simplified if we use propellant grains obtained from cartridge-loaded motors. Subsequent efforts will address the more complex issues related to removing propellant from case-bonded motors. Of the 93,200 motors in the 21 lots, only 16,940 motors are case-bonded. A search for case-bonded motors with double base propellant and motors with N-5 double base propellant was conducted to identify rocket motors for demonstrations of cryocycling. Rocket motors with N-5 propellant are of interest because its formulation is similar to the Zuni and HVAR double base propellants for which Sandia has developed analytical models and demonstrated batch processing of HVAR motors. The motors identified were compared with motors available in the Orange Book, however, none of the motors were in the demilitarization inventory as of March 1996.

TABLE 7
DoD ROCKET MOTOR DEMILITARIZATION INVENTORY *

Rocket Motor					Grain Features			
Nomenclature	Storage Location	Lot Quantity	Total Motor Weight Stored (lbs.)	Total Propellant Weight (lbs.)	Diameter x Length (in.)	Weight (lbs.)	Manufacturing Method	Type Designation
5.0 MK10-7	Red River	16,631	1,995,720	399,144	4.5 x 39.3	24.0	Cartridge loaded	JPN
5.0 MK10-7	Anniston	17,039	2,044,680	408,936	4.5 x 39.3	24.0	Cartridge loaded	JPN
5.0 MK10-7	Tooele	6,357	762,840	152,568	4.5 x 39.3	24.0	Cartridge loaded	JPN
5.0 MK10-7	Sierra	5,894	707,280	141,456	4.5 x 39.3	24.0	Cartridge loaded	JPN
5.0 MK10-7	Anniston	1,520	182,400	36,480	4.5 x 39.3	24.0	Cartridge loaded	JPN
XM42E2	Tooele	380	619,400	285,000	16.0 x 102.0	750.0	Cartridge loaded	OIO
XM42E2	Letterkenny	224	365,120	168,000	16.0 x 102.0	750.0	Cartridge loaded	OIO
M24	Letterkenny	165	1,075,800	123,750	16.0 x 102.0	750.0	Cartridge loaded	OIO
JATO MK25 MOD1	McAlester	2,254	568,509	274,988	8.7 x 40.4	122.0	Case bonded	RDS-135
JATO MK25 MOD1	McAlester	544	137,209	66,368	8.7 x 40.4	122.0	Case bonded	RDS-135
JATO MK25 MOD1	Crane	1,990	501,922	242,780	8.7 x 40.4	122.0	Case bonded	RDS-135
JATO MK25 MOD1	Crane	407	102,654	49,654	8.7 x 40.4	122.0	Case bonded	RDS-135
JATO MK7 MOD2	Hawthorne	4,448	177,920	522,640	8.8 x 40.1	117.5	Cartridge loaded	AN-584J
MK6 MOD 1	Tooele	749	139,314	53,928	9.7 x 26.5	72.0	Cartridge loaded	AN-583AF
MK6 MOD 1	Crane	1,059	185,325	76,248	9.7 x 26.5	72.0	Cartridge loaded	AN-583AF
MK6 MOD 1	McAlester	724	126,700	52,128	9.7 x 26.5	72.0	Cartridge loaded	AN-583AF
MK8-2	Tooele	572	160,160	59,202	10.6 x 26.4	103.5	Cartridge loaded	OIY
MK8-1	Hawthorne	250	114,125	25,875	10.6 x 26.4	103.5	Cartridge loaded	OIY
TOW M114	Anniston	20,315	153,492	24,378	0.8 x 13.8	1.2	Cartridge loaded	M7
MK52 E Aim 7e	McAlester	397	105,046	38,112	7.8 x 41.3	96.0	Case bonded	ANB-3109
2.75 SR 105J1	Sierra	11,348	247,764	94,188	2.7 x 19.0	8.3	Case bonded	ANB-3141-1

*Stored weight >100,000 lbs

SUMMARY AND CONCLUSIONS

The analyses described in this report along with the laboratory and pilot-scale demonstrations that were done in this study show that cryocycling is an effective, safe, and environmentally friendly means of rubblizing bulk energetic materials. We conclude that the cryocycling process is especially useful for--and is ready to be applied to--non-case-bonded, double base propellants. These propellants are found in a number of different rocket motors, and they represent a significant portion of the DoD demilitarization inventory of energetic materials. In addition, the analytical modeling and laboratory results show that cryocycling can also be applied to a wide variety of other solid propellants and high explosives.

The analytical and finite element analysis methods developed in this investigation and described above enhance our understanding of the importance of key process and energetic material parameters. These methods can therefore be used to optimize a proposed cryocycling process for any propellant or explosive that is of interest. In particular, finite element simulations of the cryocycling process as applied to rocket motor propellant grains yield insight into the cracking process by providing time sequenced "snapshots" of the stress and temperature distributions and of the cracked portions of the cross section. Such information is generally not available from test results. Specifically, the numerical simulations and the analytical model reveal why propellants with different thermal and mechanical properties have different characteristic minimum particle sizes when they are cryocycled. The model and simulations also provide valuable information about efficient cryocycling times.

A number of improvements to the simulation technique can provide even more detailed information about the cryocycling process. These improvements might include cracking elements which allow new boundary conditions to be applied as cracking progresses. With such elements, we can simulate the response of new propellant boundaries in contact with liquid nitrogen. In order to be useful, however, a new cracking function of this type must be applied to the entire computational grid. Nevertheless, before these computational improvements are made, better material property information must be obtained for the propellants of interest throughout the range of temperatures encountered in cryocycling (25°C through -196°C). These data would then be consistent with--and contribute to--the accuracy of any future cryocycling process simulation.

70

REFERENCES

1. L. Whinnery, S. Griffiths, et. al., Particle Size Reduction of Propellants by Cryocycling, SAND95-8227, Sandia National Laboratories, Albuquerque, New Mexico, May 1995.

2. S. Griffiths, J. Handrock, et. al., Cryocycling of Energetic Materials: Status Report for FY94, SAND95-8235, Sandia National Laboratories, Albuquerque, New Mexico, July 1995.

3. Peter Weiss, *Lab to get blast with plan to reuse excess rocket fuel*, Valley Times, Nov. 17, 1995.

4. H.S. Carslaw and J. C. Jaeger, Conduction of Heat in Solids, Oxford University Press, 1976.

5. J. A. Clark and R. M. Thorogood, "Heat Transfer," chapter 3 in *Cryogenic Fundamentals*, edited by G. G. Haselden, Academic Press, London, 1971.

6. B. A. Boley and J. H. Weiner, Theory of Thermal Stresses, John Wiley, 1960.

7. C. A. Daniels, Polymers: Structure and Properties, ISBN No. 87762-552-2, Technomic, Lancaster PA, 1989.

8. I. N. Sneddon and M. Lowengrub, Crack Problems in the Classical Theory of Elasticity, John Wiley, 1969.

9. A. H. Lachenbruch, "Depth and Spacing of Tension Cracks", J. Geoph. Res., 66 (12), 4273-4293, 1961.

10. L. M. Keer, S. Nemat-Nasser, and A. Oranratnachai, "Unstable Growth of Thermally Induced Interacting Cracks in Brittle Solids," Int. J. Solids Structures, 15, 111-126, 1979.

11. PRONTO3D, A Three-Dimensional Transient Solid Dynamics Program, L.M. Taylor and D.P. Flanagan, SAND87-1912, Sandia National Laboratories, Albuquerque, New Mexico, March 1989.

12. JAC2D - A Two-Dimensional Finite Element Computer Program for the Nonlinear Quasi-Static Response of Solids with the Conjugate Gradient Method, J.H. Biffle and M.L. Blanford, SAND93-1891, Sandia National Laboratories, Albuquerque, New Mexico, May 1994.

13. JAC3D - A Three-Dimensional Finite Element Computer Program for the Nonlinear Quasi-Static Response of Solids with the Conjugate Gradient Method, J.H. Biffle, SAND87-1305, Sandia National Laboratories, Albuquerque, New Mexico, February 1993.

14. Coyote II - A Finite Element Computer Program for Nonlinear Heat Conduction Problems; Part I - Theoretical Background, D.K. Gartling and R.E. Hogan, SAND94-1173, Sandia National Laboratories, Albuquerque, New Mexico, October 1994.

15. Coyote II - A Finite Element Computer Program for Nonlinear Heat Conduction Problems; Part II - User's Manual, D.K. Gartling and R.E. Hogan, SAND94-1179, Sandia National Laboratories, Albuquerque, New Mexico October 1994.

16. "New Versions of the JAC Codes", Memo form M.L. Blanford, 1517 to JAC Users, Sandia National Laboratories memorandum dated September 27, 1995.

17. Hibbitt, Karlsson, and Sorensen, Inc., "ABAQUS Users Manual", Medway, RI, 1995.

18. "Modifications of the PRONTO 3D Finite Element Program Tailored to Fast Burst Nuclear Reactor Design," D. S. Oscar, S. W. Attaway, and J. D. Miller, SAND91-0959, Sandia National Laboratories, Albuquerque, New Mexico, August 1991.

19. JAS3D, A Multi-Strategy Iterative Code for Solid Mechanics Anakysis, Release 1.2, M.L. Blanford, JAS3D Version 1.2 User Guide, Document Version 3/26/96.

20. "A Tightly Coupled Thermal-Mechanical Analysis Capability Using COYOTE II and JAS3D," Memo from S.E. Gianoulakis to Distribution, dated December 5, 1994.

21. "MERLIN II - A Computer Program to Transfer Solution Data Between Finite Element Meshes," D. K. Gartling, SAND89-2989, Sandia National Laboratories, Albuquerque, New Mexico, July 1991.v

22. Bammann, D.J., Chiesa, M.L., Horstemeyer, M.F., Weingarten, L.I., "Failure in Ductile Materials Using Finite Element Methods," in *Structural Crashworthiness and Failure*, Edited by Jones, N.and Wierzbicki, T., Elsevier Applied Science, 1993.

23. "J2D and J3D - Post Processing Codes to Calculate the J-Integral in Two and Three Dimensions," G.W. Wellman, SAND90-2717, Sandia National Laboratories, Albuquerque, New Mexico, March 1991.

24. Larson, R. S., "Calculation of Thermal Stress Profiles During Cryocycling," Sandia National Laboratories, Livermore, CA, Organization 8745 Internal Memorandum, January 17, 1994.

25. SPIA/M2g, Unit No. 386, High Energy X-8, December 1954.

26. CPIA, IHSP 75-116, "Compilation of Ultimate Tensile Property Data for Several Propellants," X-8, November 30, 1975.

27. SPIA, Technical Report FRL-TR-56, "Tensile Properties of Double-Base Propellant," X-8, Elise McAbee and Mitchel Chmura, Feltman Research Laboratories, Picatinny Arsenal, Dover, N. J., May 1962.

28. SPIA/M2g, Unit No. 9, JPN, December 1954.

29. CPIA/M2, Unit No. 1121, N-5, May 1968.

30. Defense Technical Information Center, Cold Regions Research and Engineering Laboratory, Hanover NH, Special Report 142, "Low Temperature Behavior of N-5 Propellant," D. M. Anderson, A. Tice and B. Bartizek, Alexandria, VA, January 1970.

31. Defense Technical Information Center, Technical Report, "Rocket Motor Mk 1 Mod 0 (ASROC) Type-Life Program Final Report," N-5, Alexandria, VA, May 30, 1972.

32. Defense Technical Information Center, Technical Report, "ASROC Rocket Motor Mk 37 Mod 0; surveillance of," N-5, Alexandria, VA, December 10, 1979.

33. CPIA/M2, Unit No. 1082, M8, June 1964.

34. Disassembly and Cryocycling of HVAR, ZUNI, and FALCON Tactical Rocket Motors, Sept.94-May'95. Global Environmental Solutions, June 15, 1995

35. Stinger surface-to-air missile, MARC 80, manufactured by Atlantic Research Corp.

36. Thiokol Progress Report of Projects in Support of USAF Falcon Guided Missile   Program, 16 Aug, 1957 through 15 Nov., 1957

37. Quarterly Progress Report, April - June 1957. Thiokol Chemical Corporation, Redstone Division, Redstone Arsenal, Hunstville, Alabama. Report No. 30-57.

38. PATRAN3.0,MSC/PATRAN, McNeal-Schwidler Corp., Los Angeles, CA

39. "Engineering Design Handbook, Explosives Series Properties of Explosives of Military Interest," U.S. Army Material Command, AMCP 706-177, pp 178-180, January 1971.

40. "Aerospace Structural Metals Handbook," Edited by Brown, W.F., Mindlin, H., and Ho, C.Y., CINDAS/Purdue University, 1992 Edition.

41. "Navy Explosives Handbook, Explosive Effects and Properties - Part III, Properties of Explosives and Explosive Components," Hall, T.N., Holden, J.R., NSWC Mp 88-116, Naval Surgace Warfare Center, October 1988.

42. "LLNL Explosives Handbook, Properties of Chemical Explosives and Explosive Simulants," Dobratz, B.M., UCRL-52997, Lawrence Livermore National Laboratory, March 16, 1981.

43. (a) Morgan, John, "Surveillance Evaluation of ASROC Rocket Motors MK 37 MOD 0 FY 78 (U)," 1979. (b) Anderson, Duwayne; Tice, Allen: and Bartizek, Brian, "Low Temperature Behavior of N-5 Propellant," 1970.

44. Chemical Propulsion Information Agengy/M2 Manual.

45. Resource Recovery and Disposition Handbook, Compiled by the Joint Ordnance Commanders Group, Munitions Demilitarization/Disposal Sub-Group, available from the US Army Defense Ammunition Center, Demil Technology Office, Savanna, IL.

DISTRIBUTION:

1   Lawrence Livermore National Laboratory
        HEAF
        MS L-282
        Attn: C. Pruneda
        Livermore, CA 94550

1   US Army Defense Ammunition Center
        Demil Technology Office
        Attn: SIOAC-TD
        Attn: J. Q. Wheeler
        Savanna, IL 61074-9639

1   US Army MICOM
        Propulsion directorate
        Attn: AMSMI-PR-R
        Attn: W. S. Melvin
        Redstone Arsenal, AL 35898-5249

1   US Army ARDEC
        Demil Technologies
        Attn: SMCAR-AES-P, Bldg. 321
        Attn: R. Goldstein
        Picatinny Arsenal, NJ 07806-5000

1   Thiokol Corp.
        Demilitarization Office
        MS 130
        Attn: W. O. Munson
        Brigham City, UT 84302-0689

1   General Atomics
        Attn: M. Spritzer
             J. Elliott
        3550 General Atomics Ct.
        San Diego, CA 92121-1122

1   TPL, Inc.
        Attn: H. M. Stoller
        3921 Academy Parkway North NE
        Albuquerque, NM 87109-4416

DISTRIBUTION: (continued)

1	MS 0845	J. T. Hitchcock, 2503
1	MS 9420	L. A. West, 8200
1	MS 9405	J. Hruby, 8230
1	MS 9405	L. Whinnery, 8230
1	MS 9054	W. J. McLean, 8300
1	MS 9042	C. Hartwig, 8345
1	MS 9042	S. Griffiths, 8345
1	MS 9042	R. Nilson, 8345
1	MS 9007	R.C. Wayne, 8400
1	MS 9108	E. T. Cull, 8414
1	MS 9108	D. Kasberg, 8414
5	MS 9105	J. Lipkin, 8419
1	MS 9105	H. Hirano, 8419
1	MS 9405	T. M. Dyer, 8700
1	MS 9743	E-P Chen, 8742
1	MS 9043	J. Handrock, 8742
5	MS 9043	V. Revelli, 8742
1	MS 9043	L. Weingarten, 8742
3	MS 9018	Central Technical Files, 8940-2
4	MS 0899	Technical Library, 4916
1	MS 9021	Technical Communications Department, 8815/Technical Library, MS 0899, 4916
2	MS 9021	Technical Communications Department, 8815 for DOE/OSTI